Combined Dual Emission Laser Induced Fluorescence and Particle Image Velocimetry to Resolve Temperature and Velocity

by

Alan S. Grissino

B.S., Mechanical Engineering (1994)
Worcester Polytechnic Institute

Submitted to the Department of Mechanical Engineering
in Partial Fulfillment of the Requirements for the Degree of
Master of Science in Mechanical Engineering

at the

Massachusetts Institute of Technology

February 2000

Signature of Author _____
Department of Mechanical Engineering
January 14, 2000

Certified by _____
Douglas P. Hart
Assistant Professor of Mechanical Engineering
Thesis Supervisor

Accepted by _____
Ain A. Sonin
Chairman, Department Committee on Graduate Students

Combined Dual Emission Laser Induced Fluorescence and Particle Image Velocimetry to Resolve Temperature and Velocity

by

Alan S. Grissino

Submitted to the Department of Mechanical Engineering
on January 14, 2000 in Partial Fulfillment of the
Requirements for the Degree of Master of Science in
Mechanical Engineering

ABSTRACT

This thesis presents a novel technique for simultaneously measuring temperature and velocity. Using a high intensity ultrasonic field, small spherical tracer particles are formed and infused with two distinct fluorescent laser dyes. When protected by the particle encasement, dyes not normally soluble or otherwise compatible with the flow medium can be used. The fluorescence intensity of one dye is dependent upon temperature, the scalar quantity being measured, while the other temperature independent dye is used as a reference. By separating their emissions using narrow band optical filters, whole field temperature is measured simultaneously with flow velocity. Unlike other whole-field temperature measurement techniques, this combined PIT technique can be used with either gas or liquid, and is capable of resolving temperatures over an extended range. The use of DELIF tracer particles provides a high gain for superior PIV processing while enabling the use of LIF dyes.

Development of this technique is accomplished through the derivation of analysis techniques and algorithms. The effects of particle thermal response, particle size distribution, seeding density and laser light illumination are investigated using synthetically created images. To demonstrate the technique and utilize the theory and analysis methods a cold jet entering a hot tank of water is used to obtain real Particle Image Thermometry images.

Thesis Supervisor: Douglas P. Hart

Title: Assistant Professor of Mechanical Engineering

Acknowledgements

There are many people whose support and guidance have made this research project possible. I would first like to thank my academic and thesis advisor, Professor Doug Hart, for his support, insight and approval. Doug's words of wisdom and seemingly endless supply of ideas helped to shape the body of this research and ensure that the correct issues were addressed. Through the ups and downs, we have persevered and seen this project through to a favorable end.

I would also like to thank those in the Fluid Mechanics Lab who aided in my struggle. Without the help of Hugo, most of my image files would still be on a Mac! Carlos was an excellent sounding board for my ideas on PIV and particle fluorescence. Discussions with him helped to clear several issues, and his willingness to help out and let me use his experimental setup were invaluable. I also need to thank those in the Non-Newtonian Fluids Lab for not getting too mad at me when I blew up a batch of fluorescent particles.

I would like to thank TSI Incorporated of Minnesota, for the use of their resources and time for experimentation. I thank Wing Lai for his help in coordinating the TSI/MIT effort, his help during experimentation and analysis of PIV images, and more importantly, his hospitality during my trips to the *Land of 10,000 Lakes*. Thanks to Dan Bjorkquist for his help with experimentation and his programming efforts which made my analysis easier.

Great thanks goes out to my *GE Advanced Course in Engineering* compatriots, Doug Walters, Garth Grover and Brent Brunell. From the early days of A-course through all of our classes and work leading up to this milestone, our combined support has helped to make this long road more enjoyable. Thanks also goes to my sponsor, *GE Aircraft Engines*, for their time (and money!). I would like to thank my wonderful family. The words of support and encouragement from my parents and in-laws, especially Heinz and Peta, have been invaluable.

Most importantly, I would like to dedicate this thesis to my wife and children. Without the unyielding support and unearthly patience of my wife Liza, *none* of this would be possible. It has been a long, difficult road for all, and I cannot express enough how much I appreciate her support over the past four years. It has been a true testament to the strength of our marriage and family. I thank my two wonderful boys, Jason and Evan, whose patience with Daddy doing homework all the time was very much appreciated. I love you all very much, and now may actually be able to spend some time with you!

Table of Contents

Table of Figures

Chapter 1 - Introduction

The field of experimental fluid mechanics has seen great advances in the qualitative measurement of whole field velocity through techniques such as Particle Image Velocimitry (PIV), Molecular Tagging Velocimetry (MTV), and Doppler Global Velocimitry (DGV). In many instances, however, temperature is as important, if not more so, than velocity (i.e., natural and forced convection, mixing, combustion, etc.). Several techniques for non-invasively measuring whole-field temperature have been developed, but none have taken hold and moved to the forefront as a viable and practical method for general use.

1.1 Past Research

As early as 1984, Ogden and Hendricks [1] and Rhee, Koseff and Street [2] used liquid crystals for a *qualitative* visualization of flow structures. Dabiri and Gharib [3] obtained quantitative temperature measurements with liquid crystals using computer analysis of recorded reflected light values. While their technique was very temperature sensitive, (0.01°C), they reported results for only a narrow temperature range (3°C). Nakajima, Utunomiya and Ikeda [4] obtained simultaneous measurement of velocity and temperature with separate systems. Laser Doppler Velocimetry (LDV) was used for velocity (standard Mie scattering exaggerated with 100 μm polystyrene particles) and solute Rhodamine B (RhB) for temperature. The decrease of Rhodamine B's fluorescence intensity with temperature was used to calibrate and extract scalar temperature information.

Using a concept from the field of biology and biochemistry, Coppeta and Rogers [5] studied the measurement of scalar fluid quantities (temperature, concentration, pH) using a *ratiometric* technique called Dual Emission Laser Induced Fluorescence (DELIF). Two organic fluorescent dyes are used, one dependant on the scalar being measured and the other independent. They reported on the fluorescent characteristics of several dye combinations as potential for pH and temperature measurement. More recently, Sakakibara and Adrian [6] using Rhodamine B and Rhodamine 110 as the indicators utilized a ratiometric technique similar to Coppeta and Rogers's to measure thermal convection in heated horizontal surface.

By optically filtering the emitted light they calibrated the system and reported results over a broad temperature range (20°C - 50°C).

1.2 Goals

Presented herein is a combined DELIF and PIV optical diagnostic technique, hereafter-called Particle Image Thermometry (PIT).

By embedding the dye indicators within the tracer particles used for PIV, simultaneous measurement of velocity and temperature is achieved. Embedding the dyes within tracer particles provides a means of accurately controlling dye concentrations. Furthermore, dyes do not have to be chemically compatible with or soluble in the fluid medium. Consequently, measurements can be made in both gases and liquids with dye combinations not possible when soluble dyes are required. The ability to reuse the particles minimizes the financial impact if a costly dye must be used and the environmental impact if a hazardous dye must be used. The combination of these attributes greatly improves the practicality and accuracy of PIT as a means of temperature measurement as it enables the use of a broad range of illumination sources, imaging methods, and dye combinations.

Paramount to the physical property benefits is the high gain signal that fluorescent particles provide for PIV. Indeed, the crux of this method is that the same particles used for PIV analysis are used for temperature analysis, negating the need for separate systems. The PIT data reduction and analysis can easily be incorporated into PIV software and analysis codes, providing true simultaneous calculations of velocity and temperature.

1.3 Nomenclature

General Notation

I	*Radiative intensity*	W
C	*Dye concentration*	mg/ml
V	*Volume*	m^3
ε	*dye absorption coefficient*	m^2/gm
r	*radius*	m
d	*diameter*	m
k	*thermal conductivity*	W/m^2K
θ	*angle*	*radians*
Cp	*specific heat, constant pressure*	J/kgK
Cv	*specific heat, constant volume*	J/kgK
ρ	*density*	kg/m^3
t	*time*	*sec*
T	*temperature*	*°C (or K)*
Θ	*non-dimensionalized temperature*	-
h	*heat transfer coefficient*	W/m^2K
R	*outer radius of sphere*	m
α	*thermal diffusivity*	m^2/sec
β_n	*n^{th} root of transcendental equation*	-
C_d	*drag coefficient*	-
v	*velocity*	m/s
g_c	*gravitational acceleration*	m/s^2
M	*mass*	kg
As	*surface area*	m^2
μ	*dynamic viscosity*	$N\text{-}sec/m^2$
t^*	*dimensionless time*	-
MW	*molecular weight*	mol/gm
λ	*wavelength*	nm

Subscripts

e	*exitation*
f	*fluorescence (also fluid)*
A	*camera A in dual-camera PIV setup*
B	*camera B in dual-camera PIV setup*
abs	*absorption*
em	*emmision*
o	*final or external*
i	*initial*

Non-dimensionalized Parameters

Re	*Reynolds number*
Pr	*Prandtl number*
Nu	*Nusselt number*
Bi	*Biot number*

Chapter 2 - Fluorescence

2.1 Ratiometric Technique

Fluorescence is a radiative energy process categorized as a subset of the larger phosphorescent phenomenon. Certain chemical compounds react to incident energy stimulation by absorbing energy and transferring electrons within the molecule. These movements cause an increase in the electrical potential energy of the molecule, from a stable ground state to a higher order electronic state. When the molecule returns to the ground state, energy is released, usually in the form of light. The length of time that this emitted light persists is the basis for the general categorization of fluorophors. *Fluorescence* is typically defined when the time is less than about 10^{-8} seconds.

The intensity of fluorescence is dependent upon many factors, including intensity of incident excitation energy, dye concentration, volume, and characteristics of the dye. The general equation for intensity is

$$I_f = I_e C \phi \varepsilon V, \tag{1}$$

where I_e is the intensity of the excitation beam at that point, C is the concentration of dye, ϕ is the quantum efficiency, ε is the absorption coefficient, and V is the volume.

Coppetta and Rodgers investigations used separate dyes to minimize the variable effects of laser light intensity and other potential conflicts on detecting a scalar value of interest. This *ratiometric* technique uses one dye whose fluorescence is dependent on the scalar being measured (temperature, pH, etc.) and one dye, a reference dye, that is not. As reported by Coppetta et al., the ratioing concept is an established technique in the cellular biology field (Bassnett et al [7], Morris [8], and Parker et al. [9]).

This technique involves taking a ratio of the fluorescence intensity Equation (1) for each dye. We obtain,

$$\frac{I_{fA}}{I_{fB}} = \frac{I_e C_A \phi(T)_A \varepsilon_A V}{I_e C_B \phi(T)_B \varepsilon_B V} = \frac{C_A \phi(T)_A \varepsilon_A}{C_B \phi(T)_B \varepsilon_B} \tag{2}$$

Equation (2) shows that the fluorescence ratio of the dyes is only a function of dye concentration, quantum efficiency, and absorption coefficient. The ratio has eliminated the laser sheet intensity. For the dye combination in the present investigation, the quantum efficiency (ϕ) is the significant temperature dependent property. For the ratioing analysis to be accurate and viable, the incident laser intensity used to measure the fluorescence of the two dyes must be approximately equal. This is generally not possible with a single camera using a pulsed laser. However, it can be accomplished using a scanning Continuous Wave (CW) laser system with color wheel filter. It can also be done using a two-camera stereo PIV system with optical filters as in the current study. The fluorescence from both dyes is then recorded at the same time.

Recent studies of film thickness using LIF show that absorption of Rhodamine B *may* exhibit a temperature dependency. However, the author has only seen qualitative proof of this phenomenon, and the experiments performed are being done at high temperatures (200+ °C). As seen in Figure 1, Coppetta and Rogers show that Rhodamine B absorption is essentially temperature independent for the temperature range of interest in this research (20-60°C).

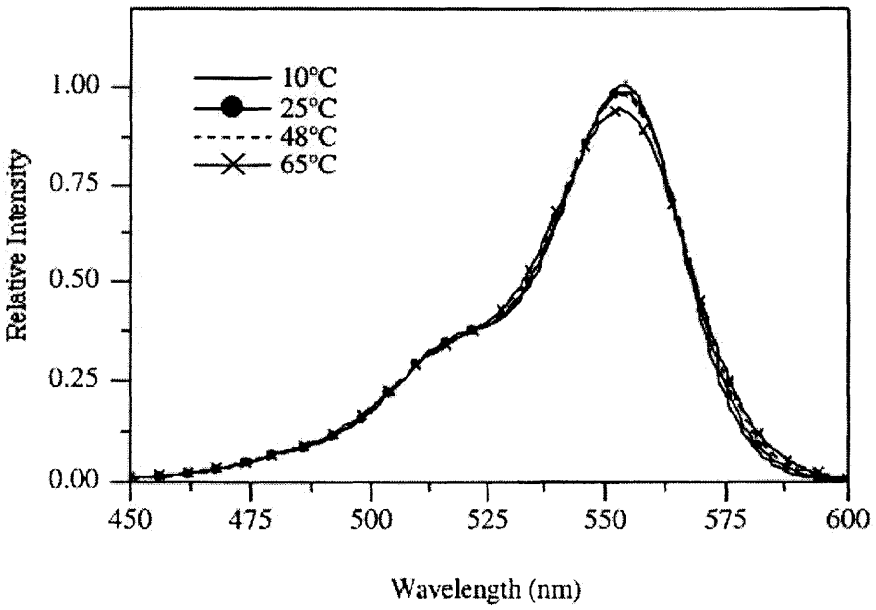

Figure 1 - Rhodamine B Absorption Spectrum vs. Temperature

2.2 Dye Selection and Characteristics

The selection of a proper fluorescent dye combination for this technique is dependent on many experimental design considerations. These include the flow medium of interest, type of flow field, and others. The temperature dependent dye used in the present investigation is Rhodamine B known for it's strong dependence on temperature (about 2.3%/°K). Rhodamine B has been widely used in LIF studies due to its solubility characteristics and temperature dependence. With a peak absorption at around 556 nm, it is easily excited by either a frequency doubled Nd:YAG laser (532 nm) or the 514 nm line of an argon-ion laser. The peak emission of Rhodamine B occurs at approx. 580 nm.

The reference, temperature independent dye chosen is Pyrromethene 650 (PM650) (1,2,3,5,6,7 - hexamethyl - 8 - cyanopyrromethene - difluoroborate complex, or BF_2 - complex). Pyrromethene 650 has a peak absorption around 588 nm (in Ethanol) and a peak emission at 625 nm. Although it's thermal stability is exceptional, it is not soluble in water. Table 1 shows properties for various dyes.

Table 1 - Dye Characteristics

Dye -	MW mol/g	λ_{abs} nm	λ_{em} nm	ϕ -	ε m^2/g
PM650	301.15	588	624	0.54	0.0183
RhB	479.02	556	580	0.31	4.4
Rh110	366.80	496	520	0.80	34

2.3 Spectral Conflicts and Image Overlap

Copetta and Rogers discuss three spectral type conflicts when using two fluorescent dyes. Their *Type II* conflict occurs when there is an overlap in the absorption band of one dye with the emission band of the other. Figure 2 illustrates an example of this type of interaction. This conflict results in the measured fluorescence of dye 1 being less than the actual emission, due to it being absorbed by dye 2 as it travels through the medium. However, for a constant path length, a calibration curve that is *independent* of path length can be constructed

by dividing the fluorescence ratios at all temperatures by the ratio at some arbitrary reference value.

Such a Type II conflict exists when Rhodamine B and Pyrromethene 650 are used in combination. Despite this conflict (which can be overcome), PM650 was selected partially to illustrate the utility of a non-compatible (soluble) dye.

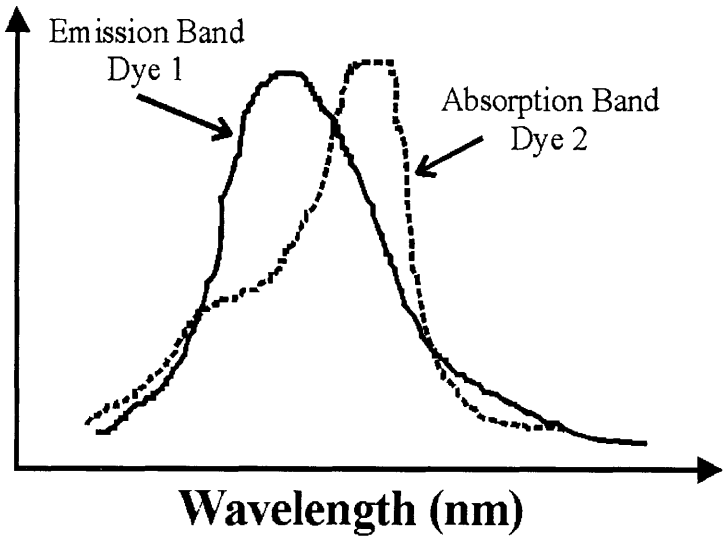

Figure 2 - Illustration of Spectral Overlap Conflict. Y-axis is relative absorption/emission in arbitrary normalized units.

2.4 Dye Concentration Ratio Effects

Equation (2) shows that the intensity ratio is a function not only of temperature (through the quantum efficiency ratio), but also of the ratio of dye concentrations. In its simplest form this relationship is linear. Adrian & Sakakibara [6] accounted for imperfect separation of the two dye intensities, I_A and I_B. Overlapping emission bands of the two dyes may cause some fraction of the light I_A to be detected by camera B, and likewise, a fraction of light I_B detected by camera A. Equation (2) can be reformulated to address this issue, as done by Adrian et. al. The equation they arrive at takes this imperfect light filtering into account, through careful calibration of the image capture and optical system. This equation is

$$\frac{V^{\alpha}}{V^{\beta}} = \frac{C_{A/B}C'_{B}\phi_{A}\phi'_{B}V^{\alpha}_{C_B=0} + C'_{A}\phi_{B}\phi'_{A}V^{\alpha}_{C_A=0}}{C_{A/B}C'_{B}\phi_{A}\phi'_{B}V^{\beta}_{C_B=0} + C'_{A}\phi_{B}\phi'_{A}V^{\beta}_{C_A=0}} . \quad (3)$$

Experimental results for the two dyes used in their procedure (Rhodamine B and Rhodamine 110) are shown in Figure 3 by the curve-fit line and open symbols. Their evaluation of Equation (3) very closely matches the experimental results shown here. The solid line in the figure represents Equation (2) evaluated using the physical properties for RhB and Rh110 found in Table 1. As noted, this is a linear relationship. The experimental results (and prediction from Equation (3)) show the introduction of a nonlinear power relationship in the form $Y = aX^b$. Adrian et. al., reason that an optimum value of V^{α}/V^{β} is obtained when the signal-to-noise (S/N) ratio of each camera is the same. This is because the measurement of V^{α}/V^{β} can not have a S/N ratio higher than that of the lower S/N ratio a single camera, A or B. Put another way, the S/N ratio of V^{α}/V^{β} is maximized when the S/N ratio of V^{α} and V^{β} are equal. Since the camera gain (sensitivity) of each camera was set to the same, this criteria is met when $V^{\alpha}/V^{\beta} = 1$.

The measured data in Figure 3 shows that this occurs at a concentration ratio C_A/C_B of approximately 20. This agrees very well with the theoretical linear calculation, which also crosses 1.0 at exactly C_A/C_B of 20.

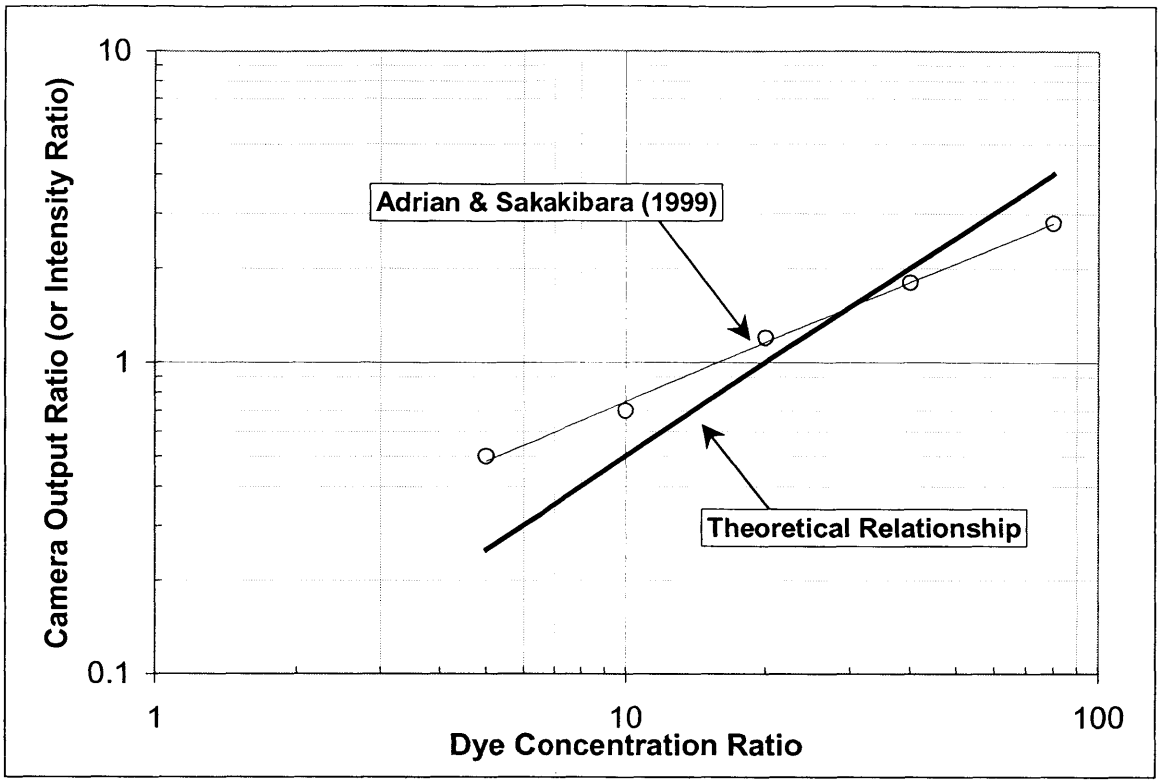

Figure 3 *- Dye Concentration Ratio Effects*

Chapter 3 - Particle Manufacture

3.1 Overview

A key aspect technique presented here is the infusion of two separate fluorescent dyes into the spherical tracer particles used for PIV. As reported by Frigerio [10], tracer particles for use in PIV applications must "...meet to very specific size, shape, density, and fluorescence requirements." There are very few commercial manufacturers of fluorescent tracer particles for such applications, and those that do exist charge as much as $250 per gram. This cost barrier prompted Frigerio and Hart to develop a manufacturing process for particles using their own internal equipment and labor resources. The trials of this initial effort are provided in Frigerio's thesis. The result of their efforts was particles made from a polyester monomer resin, linked with an external catalyst. The fluorescent dye was embedded in the particles during their creation. The approach is based on the fact that the surface tension properties of the resin causes spherical beads to be formed when placed into water. Frigerio's technique was utilized and modified for use in manufacturing PIT fluorescent tracer particles.

3.2 Particle Manufacturing Technique

The particle making procedure was resurrected for this research project, and successful batches of Rhodamine G (RhG) particles were made. However, creation of particles with *two* different fluorescent dyes proved to be more challenging. The fact that Pyrromethene 650 (PM650) is not water-soluble apparently adversely affected the resin curing process. Investigation revealed that the PM650 did not appear to be staying in solution with the resin at all. Many attempts were made using different concentrations of catalyst, dyes, and anti-emulsifying agents. Limited success was realized when the PM650 was first mixed with methanol, a substance in which it *is* soluble. This approach produced a usable batch for the current research, and the manufacturing process is reported here. It is noted that even at the time of this printing, research is ongoing in the Fluid Mechanics Laboratory at MIT to perfect the process of dual dye tracer particle manufacture.

Particles used here are manufactured from a catalyzed polyester and styrene monomer resin. Using the cavitation effects from a high intensity ultrasonic generator, the large spheres formed by the resin in the water solution are "hammered" apart. In combination with a magnetic stir bar, the power level and duration of the ultrasonic device (sonicator) are varied to produce desired particle size distributions. Through further sifting and sieving after the curing process is complete, controlled distributions with sizes ranging from less than 10 μm up to 100 μm (and larger) in diameter are created.

The following procedure outlines the ingredients and steps used to create the dual dye particles used for the current research.

1. Ingredients:
   0.7 gm Sodium Chloride, NaCl
   0.2 gm Ammonium Thyocianate
   0.5 gm Polyvinyl Alcohol (PVA)
   5 mg Pyrromethene 650 (PM650)
   100 mg Rhodamine B
   Distilled water
   25 ml methanol
   100 ml polyester casting resin
   Casting resin catalyst (methyl-ethyl-ketone-peroxide, MEKP)

2. Pour the 25 ml of methanol into a 50 ml or larger glass beaker. Add the 5 mg of PM650 dye. Mix well.

3. Pour the 100 ml of casting resin into a 150 ml or greater glass beaker. Add the PM650/methanol mixture and stir very well. Let the mixture stand until the methanol has evaporated from the mixture (about 1 hour).

4. While the resin mixture is evaporating, pour 400 ml of distilled water into a 500 or 600 ml glass beaker.

5. Place the beaker of water on a combination hot plate/magnetic stirrer. Begin to heat the water while mixing with a mag. stir bar.

6. Measure and add the Sodium Chloride, Ammonium Thiocynate and Polyvinyl Alcohol to the water. While still mixing, heat to approx. 50°C.
7. When the resin mixture has returned to the original 100 ml level (i.e., all of the methanol has evaporated off), proceed to next step.
8. Transfer the resin mixture into a 500 or 600 ml glass beaker. Add 20^{+} drops of catalyst (MEKP) to resin mixture and stir vigorously for 30 sec., taking care to scrape the sides and ensure extremely well combination.

   NOTE: addition of the catalyst will begin the chemical reaction to bind the polymer chains in the resin. It will start to become stiff very rapidly, so this step and the following must be performed *quickly*.
9. Place the resin beaker on the hot plate and *very quickly* pour in the water solution, stirring vigorously. With the mag. stirrer operating, *quickly* place the sonicator horn into the mixture.
10. Run the sonicator on HI continuous power setting for 2 min 30 sec.
11. Heat the mixture to 70°C while mixing with stir bar. Turn off or remove from heat and allow to cool back down to 30-50°C.
12. Repeat step 11 twice.
13. With heat off, stir for approx. 10 hours while particles are curing. (The heating and cooling cycles of steps 11 and 12 speed up the chemical reaction).

The particles are cured now ready to be separated.

Using appropriate fine mesh metal sieves, filter and separate the particles to the desired sizes. Once sieved, add denatured alcohol to the particles and place back on stir-pad. Let stir in the alcohol for 10 hours. The particles should now be fully cured and bleached of any excess dye.

3.3 Results of Particle Manufacture

The above recipe and procedure results in remarkably spherical tracer particles, suitable for both normal PIV processes and the current PIT process. Figure 4 shows typical particles. The magnification is approximately 100X.

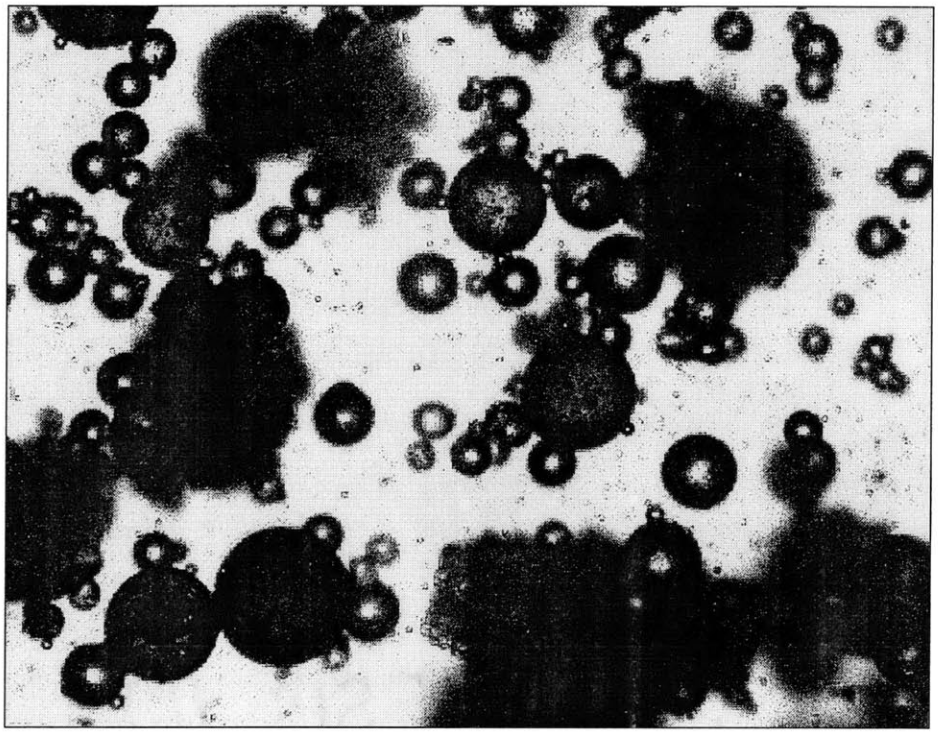

Figure 4 *- Spherical tracer particles with PIT dyes infused. Magnification is approximately 100X*

Figure 5 illustrates the type of size distribution represented by the particles in Figure 4 above.

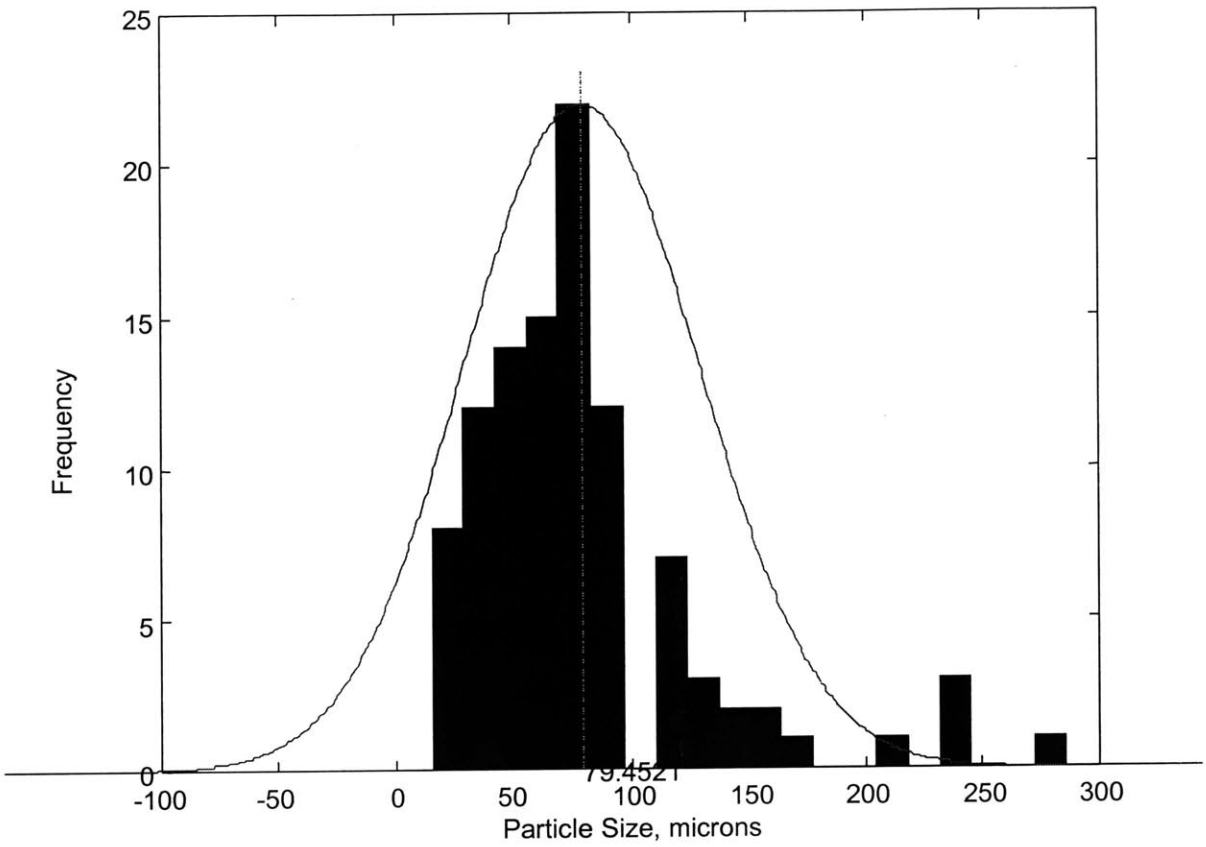

Figure 5 - Representative Particle Size Distribution. Based on Figure 4.

Chapter 4 - Particle Thermal Time Response

4.1 Background

The PIT technique is reliant upon several assumptions about the physical system involved. Past experiments have utilized fluorescent dyes in aqueous solution. In solution, the dye molecules are an integral part of the water, and as such, will respond to changes in temperature in a time span on the same order of magnitude as the water. Therefore, the fluorescence at a point in the water at any given time truly is an indicator of the temperature of the water at that point.

In the technique presented here, the dye is embedded in small spherical particles made of plastic. While the particles are very small (10-100 μm), they are still orders of magnitude larger than the surrounding water molecules. The particle will therefore have a finite thermal lag. Knowledge of this time lag, or thermal response time, is necessary when determining the size, scope, accuracy and materials for a given experiment. If the time response is much larger (order of magnitude) than either the presumed temperature and velocity time scale of the flow field or of the image capturing system, the results could be erroneous. The particles fluorescence indicates it's temperature at that instant in time, so if the particle has not reached nearly the same temperature as the surrounding fluid, then it will not represent the temperature of the fluid.

Having established that the particles exhibit a finite, perhaps relatively large thermal response time, it is the goal of the following chapter to provide both mathematical and physical meaning to the solution(s) of this problem.

4.2 Physical System Model

The problem presented here is one of a spherical particle immersed in a fluid (water in this case). As demonstrated in the previous section and shown in Figure 4, the spherical

assumption is valid. The next step is determining what boundary conditions are imposed on the spherical particles. This is a crucial step, as it governs both the mathematical solution and the physical interpretation of the resulting thermal time response.

For the given system of plastic particles in water, only conduction and convection will be considered as potential dominant modes of heat transfer. Described herein are several potential modeling situations which may (or may not) be viable representations of the particles. Subsequently, assumptions are applied and the mathematical formulation of each solution is derived and solved. Results are presented and argument is made for the most probable approach that models the real physical system.

All of the following analyses are based on the heat conduction equation for a sphere. Combining Fouriers Law of Conduction with a control volume energy balance leads to the complete heat conduction equation (expressed in spherical coordinates). This is

$$\frac{1}{r^2}\frac{\partial}{\partial r}\left(kr^2\frac{\partial T}{\partial r}\right)+\frac{1}{r^2\sin\theta}\frac{\partial}{\partial\theta}\left(k\sin\theta\frac{\partial T}{\partial\theta}\right)+\frac{1}{r^2\sin^2\theta}\frac{\partial^2}{\partial\phi^2}(kT)+\dot{q}=\rho c_v\frac{\partial T}{\partial t}. \qquad (4)$$

With the assumption that the heat flow is one dimensional (radial) and that the fluid properties are constant in both time and space, Equation (4) is reduced to

$$\frac{\partial T}{\partial t}=\frac{1}{r^2}\cdot\frac{k}{\rho c_p}\cdot\frac{\partial}{\partial r}\left(r^2\frac{\partial T}{\partial r}\right). \qquad (5)$$

This equation is subject to an initial condition (temporal) and a boundary condition (spatial) at the surface. Temperature is a function of both time t and radius r. Solution of the differential equation varies by type of boundary conditions applied, but methods are prescribed in Carslaw and Jeager [11] and Schnieder [12].

4.2.1 Convection

4.2.1.1 Background

When posed with a situation of a solid material in contact with a fluid, as presented here, it is usually assumed that a *convection* boundary condition is present. The interaction of the fluid boundary layer and the solid surface at the contact interface dictates the mode of energy transport. Whether the movements of the shear layer at the interface is controlled by free or forced movement of the fluid far field, a *heat transfer coefficient (h)* inevitably enters the picture. The transient thermal solution of the sphere in such an environment is thus dictated by not only the environment temperature, but also by this heat transfer coefficient. This h along with the physical properties of the solid and fluid govern the flow of energy to and from the particle (and the fluid).

For the present system, it is arguable that there is a convection environment surrounding the particle. One major assumption in PIV analysis is that the particles do not disrupt the flow, and being close to neutrally buoyant, follow the fluid. Using the particles for thermometry, only fluid in the immediate vicinity of the particle is considered since the particle's fluorescence is meant to indicate the fluids temperature at that point in space. By combining these assumptions, it can be said that the particle has no relative motion with respect to the fluid, at least in close proximity to the particle. Convection heat transfer is by definition entirely dependent upon this relative motion. Therefore, it can be argued that convection is not the appropriate model for this system.

4.2.1.2 Physical and Mathematical Analysis

Despite the argument presented above, the convection solution is presented for comparison. Here, T_i is a known temperature at time $t=0$. The convection boundary condition is

$$-k\frac{\partial T}{\partial r} = h_o(T - T_o) \qquad at\ r = r_o. \tag{6}$$

This condition states that the conductive heat flux at the surface is equal to the convective heat flux away from the surface. Here, T is the surface temperature of the sphere and T_o is the environment temperature in the surrounding fluid. As outlined in Schnieder et. al., the solution of this equation takes form through a Fourier Series analysis. The solution is

$$\Theta(r,t) \equiv \frac{T(r,t) - T_o}{T_i - T_o} = \sum_{n=1}^{\infty} \left\{ \left[\frac{4(\sin\beta_n - \beta_n \cos\beta_n)}{2\beta_n - \sin(2\beta_n)} \right] \cdot \frac{R}{r\beta_n} e^{-\left(\frac{\beta_n^2 \alpha t}{R^2}\right)} \cdot \sin\left(\frac{r\beta_n}{R}\right) \right\}, \tag{7}$$

where β_i are the roots of the transcendental equation

$$1 - \beta_n \cot\beta_n = Bi = \frac{h_o R}{k}. \tag{8}$$

Because the particle temperature is a function of not only time but radius as well, it is likely that the particle will have a varying fluorescence during it's transient cooling (or heating) process. However, for the purposes of calculating the thermal response time it is appropriate to use a volume averaged temperature solution rather than the full radial dependent equation. This presumption is further supported by the assumption that the fluorescent dyes are considered homogeneously mixed throughout the spherical particle. This volume averaging is accomplished by taking the integral of the temperature over the entire sphere, and dividing by the total volume, as

$$T(t)_{AVG} = \frac{4\pi \int_0^R T(r,t) r^2 dr}{\frac{4}{3}\pi R^3} \tag{9}$$

Or, substituting the definition of normalized temperature, Θ, as defined in Equation (7),

$$\Theta(t)_{AVG} = \frac{4\pi \int_0^R \Theta(r,t) r^2 dr}{\frac{4}{3}\pi R^3} \tag{10}$$

The mathematics of solving Equation (10) can be seen in Appendix A. The result is

$$\Theta(t)_{AVG} = 3\left\{\sum_{n=1}^{\infty}\left(\frac{C_n \sin(\beta_n)}{\beta_n{}^2}\right) - \sum_{n=1}^{\infty}\left(\frac{C_n \cos(\beta_n)}{\beta_n}\right)\right\} \tag{11}$$

where

$$C_n = \frac{1}{\beta_n}\left[\frac{4(\sin\beta_n - \beta_n \cos\beta_n)}{2\beta_n - \sin(2\beta_n)}\right] e^{-\left(\frac{\beta_n{}^2 \alpha t}{R^2}\right)} \tag{12}$$

4.2.1.3 The Forced Convection Heat Transfer Coefficient

The convection solution now established, it is seen that the last unknown quantity is the heat transfer coefficient. The solution in Equation (11) is valid for any sphere in a convection environment whether forced or free. The problem now posed is how to arrive at an appropriate heat transfer coefficient to use. Two candidate *h*'s are presented here, mostly for illustrative purposes. Forced convection is used for one and free convection for the other.

Both methods will show that a heat transfer calculation for this situation not only stretches the bounds of the assumptions, but also yields results analogous to an extremely forced convection flow situation, which has been posited not to make physical sense here.

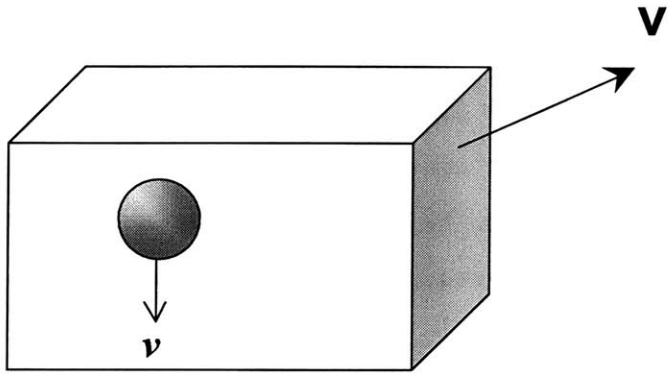

Figure 6 - Particle Relative Velocity Motion

Again, it is stated that the convection analysis presented here goes against the earlier statement that the particle is *not* in relative motion with respect to the fluid surrounding it, and therefore can have not convection. The first convective heat transfer coefficient calculated is based on the particle "falling" through the liquid. Assume that while the particle may in fact be moving with the surrounding fluid, it is slowly falling through this control volume. Figure 6 illustrates this.

The rectangular control volume represents a small region of fluid moving with a local bulk velocity of **V**. The particle is moving with this bulk piece of fluid, but at the same time is "falling" through it, due to it's slightly different density. It can be shown that this velocity $\boldsymbol{v}$ is much smaller in magnitude than the bulk local velocity, **V**, and that in a typical PIV frame sequence (~ 33ms), the particle will fall less than half of its diameter. Therefore, this approach should not introduce error into the analysis.

In the worst case situation, the particle will fall at it's terminal velocity, or the point when it's weight (buoyant force) is matched by its' drag force. For a given particle size, density, and fluid, this force balance can be solved for the velocity $\boldsymbol{v}$. This velocity is then

used to calculate a Reynolds number, a Nusselt number, and finally, a heat transfer coefficient $\boldsymbol{h}$. As the following equations show, the procedure to calculate the velocity is an iterative one, because the drag coefficient is a function of Reynolds number. The equations are

$$\underbrace{\frac{1}{2}C_D\rho v^2\frac{\pi}{4}D^2}_{DragForce}=\underbrace{\frac{\pi}{6}D^3(\rho_f-\rho)g_c}_{BuoyantForce}, \tag{13}$$

where

$$C_D=0.4+\frac{24}{\mathrm{Re}_D}+\frac{6}{1+\mathrm{Re}_D^{0.5}}, \tag{14}$$

and

$$\mathrm{Re}_D=\frac{\rho vD}{\mu}. \tag{15}$$

For a given particle size, D, and material, and a given flow medium, the above equations are iterated to determine the terminal velocity, v, and through Equation (15), the corresponding Reynolds number. The next step is to determine the heat transfer coefficient. For flow over a sphere, a general correlation posed by Whitaker [13], and seen in most fundamental heat transfer texts is

$$\overline{Nu}_D=2+\left(0.4\,\mathrm{Re}_D^{0.5}+0.06\,\mathrm{Re}_D^{2/3}\right)\cdot\mathrm{Pr}^{0.4}. \tag{16}$$

It turns out that for the free-fall flow situation presented here, and the extremely small magnitude of the particle size, that the Reynolds number is below the applicable range of this correlation. For illustrative purposes however, this correlation is used. Lastly, to obtain the heat transfer coefficient, the definition of Nusselt number (Nu) is employed.

$$\overline{Nu}_D = \frac{h \cdot D}{k_f} \quad \Rightarrow \quad h = \frac{\overline{Nu}_D \cdot k_f}{D}. \tag{17}$$

For plastic particles in water over a size range from 10-80 μm, the average heat transfer coefficient is on the order of 10,000-50,000 BTU/hr-ft^2-°F. The low Reynolds number combined with the small diameter aid in making this h very large. This h is used in Equation (8) for the Biot number (Bi), which in turn governs the transient solution.

4.2.1.4 The Free Convection Heat Transfer Coefficient

An analysis is also performed assuming a free convection environment around a sphere. Free convection currents are driven by a temperature difference between the surface of the object and the surrounding fluid. The analysis therefore becomes more difficult for the transient case, as the formulation for a free convection heat transfer coefficient is dependant upon the temperatures of the environment and the spherical surface, which is not necessarily know a-priori. An iterative approach is an acceptable method for a steady state analysis, but begins to fall apart when attempting a transient solution. If the transient changes to the surface and boundary temperature are assumed minimal and a steady state approach used to arrive at a heat transfer coefficient, the problem is manageable. This analysis was performed, with the resultant h_{free} on the same order of magnitude as the forced convection h from the previous section. Typical values for a moderate temperature difference and 10-50 μm particles is in the range of 10^4 BTU/hr-ft^2-°F.

4.2.2 Conduction

Three more system models for determining the transient thermal behavior of the particle are presented here, two of which are truly a conduction solution, while the other is based on an energy balance approach. Again, the situation is described, assumptions stated, and mathematical solution presented.

4.2.2.1 Imposed Constant Surface Temperature

Equation (5) is used again as the governing differential equation to be solved. The sphere is initially at temperature T_o, and its surface (at $r=R$) suddenly changed to *and maintained at* T_i for time greater than zero. While the mathematics is different, the physical interpretation of this situation is similar to that of an infinite (or extremely large) convective heat transfer coefficient. In such a case, the surface would take on the environment temperature very quickly, and remain there. The solution to the conduction equation with this boundary and initial condition as given by Schnieder is

$$\Theta(r,t) \equiv \frac{T(r,t)-T_o}{T_i-T_o} = \frac{2}{\pi}\cdot\left(\frac{R}{r}\right)\cdot\sum_{n=1}^{\infty}\sum_{n=1}^{\infty}\left[\frac{(-1)^{n+1}}{n}e^{-(n\pi)^2\left(\frac{\alpha t}{R^2}\right)}\cdot\sin\left(n\pi\frac{r}{R}\right)\right]. \quad (18)$$

Using the same approach as outlined in the convection section, Equation (18) is used to derive a volume average solution. Again, the mathematics can be seen in Appendix A. The resultant equation is

$$\Theta(t)_{AVG} = \frac{6}{\pi}\left\{\sum_{n=1}^{\infty}\left(\left(\frac{1}{n\pi}\right)^2\cdot D_n\sin(n\pi)\right)-\sum_{n=1}^{\infty}\left(\left(\frac{1}{n\pi}\right)\cdot D_n\cos(n\pi)\right)\right\}, \quad (19)$$

Where D_n is defined as

$$D_n = \frac{(-1)^{n-1}}{n}\cdot e^{-(n\pi)^2\cdot\frac{\alpha t}{R^2}}. \quad (20)$$

This representation was previously used by the author in a paper presented at *the 3rd Annual PIV Workshop* in Santa Barbara, CA in September of 1999. Upon further analysis and

interpretation, it is now seen that this model of the system is most likely incorrect. Again, the results are postponed until all scenarios are described and the mathematics presented.

4.2.2.2 Composite Spherical Solids in Conduction

Another conceptual way to approach this physical situation is to assume that the plastic particle is encased in a structure of water (or other fluid). The assumption in this case is that the fluid acts just as any other solid material that may encase the particle. Just as in the particle itself, there exist temperature gradients in the surrounding material, which affect the response of the particle.

Carslaw and Jeager present the solution of a solid sphere of radius R_2 with an inner concentric 'core' sphere of radius R_1. Both spheres are assumed to be of a solid material, with different physical properties. Both spheres are initially at a temperature T_o, and the external temperature is zero. There is no contact resistance at the interface between the two spheres. For our case, the inner core represents the particle and the outer represent the surrounding fluid. The overall solution becomes more advanced, as there are now two coupled bodies to consider. For this composite sphere, the governing differential equations are (using the notation $u_x = rT_x$)

$$\frac{\partial u_1}{\partial t} = \alpha_1 \cdot \frac{\partial^2 u_1}{\partial r^2} \quad , \quad 0 \le r < R_1, \quad t > 0 \tag{21}$$

and,

$$\frac{\partial u_2}{\partial t} = \alpha_2 \cdot \frac{\partial^2 u_2}{\partial r^2} \quad , \quad R_1 < r < R_2, \quad t > 0. \tag{22}$$

In this situation, there are two second-order differential equations. Therefore, we need to have four boundary/initial conditions. These conditions are as follows:

$$u_1 = u_2 \quad , \quad r = R_1, t > 0, \tag{23}$$

$$u_2 = 0 \quad , \quad r = R_2, t > 0, \tag{24}$$

$$u_1 = u_2 = rT_o, \quad t = 0, \tag{25}$$

$$k_1\left(\frac{1}{r}\frac{\partial u_1}{\partial r}-\frac{u_1}{r^2}\right)=k_2\left(\frac{1}{r}\frac{\partial u_2}{\partial r}-\frac{u_2}{r^2}\right),\ r=R_1,\ t>0. \tag{26}$$

Utilizing these conditions, the equations are solved. The solution for the inner sphere (i.e., the particle in our case) is given as,

$$T(r,t)=\frac{2R_2T_o}{r}\cdot\sum_{n=1}^{\infty}\left\{\frac{e^{-\alpha\beta_n^2 t}}{\phi(\beta_n)}\cdot\sin(R_1\beta_n)\cdot\sin(r\beta_n)\cdot\sin(\varepsilon\beta_n(R_2-R_1))\right\} \tag{27}$$

where β_n are the root of the transcendental equation

$$k_2\{\varepsilon R_1\beta\cot(\varepsilon\beta(R_2-R_1))+1\}+k_1\{R_1\beta\cot(R_1\beta)-1\}=0. \tag{28}$$

Also,

$$\phi(\beta_n)=\sigma R_1\beta_n\sin^2\{\varepsilon\beta_n(R_2-R_1)\}+\varepsilon\beta_n(R_2-R_1)\sin^2\{\beta_n R_1\}+\frac{1-\varepsilon\sigma}{\varepsilon R_1\beta_n}\cdot\sin^2\{\beta_n R_1\}\cdot\sin^2\{\varepsilon\beta_n(R_2-R_1)\} \tag{29}$$

and

$$\varepsilon=\sqrt{\frac{\alpha_1}{\alpha_2}},\quad \sigma=\frac{k_1}{\varepsilon k_2}. \tag{30}$$

Again, the volume average solution is obtained by integrating Equation (27) over the sphere. The details are contained in Appendix D. The solution in terms of the normalized temperature $\Theta(t)_{AVG}$ is,

$$\Theta(t)_{AVG}=1-\frac{6R_2}{R_1^3}\cdot\left\{\sum_{n=1}^{\infty}\left\{\frac{e^{-\alpha\beta_n^2 t}}{\beta_n^2\cdot\phi(\beta_n)}\cdot\sin^2(R_1\beta_n)\cdot\sin(\varepsilon\beta_n(R_2-R_1))\right\}-R_1\cdot\sum_{n=1}^{\infty}\left\{\frac{e^{-\alpha\beta_n^2 t}}{\beta_n\cdot\phi(\beta_n)}\cdot\sin(2R_1\beta_n)\cdot\sin(\varepsilon\beta_n(R_2-R_1))\right\}\right\} \tag{31}$$

As can be seen, this solution is much more complex than the others presented here. While solvable, it most likely does not represent well the physical situation at hand. Part of the assumptions made about PIT as explained in previous sections, is that in the near vicinity of the particles there is no temperature gradient. This equation is solved and presented with the other solutions in the following sections.

4.2.2.3 Sphere in Contact with a Well-Stirred Fluid

The last model to investigate is that of a sphere immersed in a fluid bath. In this situation, the fluid is considered to be in a 'well-stirred' state; that is, there is no temperature gradient in the fluid immediately surrounding the sphere. The mass of fluid around the sphere is assumed to have no heat loss to the surroundings. The boundary condition in this instance is therefore a simple energy balance between the sphere and fluid. The heat (energy) conducted to the surface results in a net energy rise in the fluid. Mathematically, this boundary condition at $r = R$ is given by

$$-A_s \cdot k_p \cdot \frac{\partial T}{\partial r} = M_f Cp_f \frac{\partial T}{\partial t}, \qquad t > 0. \tag{32}$$

The added assumption here is that for time t > 0, the surface temperature of the sphere is equal to that of the fluid. Unlike the previous analysis in Section 2.2.2.1 however, this surface temperature changes with time, as the energy balance continues. Again, the governing partial differential equation is solved using the above boundary condition. The equation is solved with the convention that the fluid is initially at zero temperature. The result is

$$T(r,t) = \frac{T_o}{\varepsilon + 1} - \frac{2\varepsilon R T_o}{3r} \cdot \sum_{n=1}^{\infty} \left\{ e^{-\alpha \beta_n t} \cdot \frac{\varepsilon^2 (R\beta_n)^4 + 3 \cdot (2\varepsilon + 3) \cdot (R\beta_n)^2 + 9}{\varepsilon^2 (R\beta_n)^4 + 9 \cdot (\varepsilon + 1) \cdot (R\beta_n)^2} \cdot \sin(R\beta_n) \cdot \sin(r\beta_n) \right\} \tag{33}$$

Here, β_n are the roots of the transcendental equation

$$\tan(R\beta) = \frac{3(R\beta)}{3+\varepsilon\cdot(R\beta)^2}, \tag{34}$$

and ε is defined as

$$\varepsilon = \frac{M_f Cp_f}{M_p Cp_p}. \tag{35}$$

It is seen by inspection that for very large times t (i.e., steady state), the exponential term decays to zero and the remaining solution at t → ∞ then is simply a steady state energy (enthalpy) balance of the system. Writing this energy balance mathematically gives

$$T_{of} M_f Cp_f + T_o M_p Cp_p = T\cdot\left(M_f Cp_f + M_p Cp_p\right) \tag{36}$$

Here, T is the final steady state temperature of the entire system (both sphere and fluid attain the same temperature). Using Carslaw and Jeagers convention that the initial fluid temperature T_{of} is zero, and solving Equation (36) for T with some algebraic manipulation, we get

$$T = \frac{T_o M_p Cp_p}{M_f Cp_f + M_p Cp_p} = \frac{T_o}{\dfrac{M_f Cp_f}{M_p Cp_p}+1} = \frac{T_o}{\varepsilon+1} \tag{37}$$

As stated, the transient solution in Equation (33) collapses to this steady state energy balance for very large times, as it should. The volume averaged temperature solution is now obtained, using the same procedure as before. This solution is

$$T(t)_{AVG} = T_o\left\{\frac{1}{\varepsilon+1} - \varepsilon\cdot\sum_{n=1}^{\infty}\left[\frac{1}{\beta_n}e^{-\alpha\beta_n^2 t}\cdot\frac{\varepsilon^2(R\beta_n)^4+3\cdot(2\varepsilon+3)\cdot(R\beta_n)^2+9}{\varepsilon^2(R\beta_n)^4+9\cdot(\varepsilon+1)\cdot(R\beta_n)^2}\cdot\left(\frac{2}{\beta_n R^2}\sin^2(R\beta_n)-\frac{1}{R}\sin(2R\beta_n)\right)\right]\right\} \tag{38}$$

or, in terms of the normalized temperature,

$$\Theta(t)_{AVG} = 1-(\varepsilon+1)\cdot\sum_{n=1}^{\infty}\left[\frac{1}{\beta_n}e^{-\alpha\beta_n^2 t}\cdot\frac{\varepsilon^2(R\beta_n)^4+3\cdot(2\varepsilon+3)\cdot(R\beta_n)^2+9}{\varepsilon^2(R\beta_n)^4+9\cdot(\varepsilon+1)\cdot(R\beta_n)^2}\cdot\left(\frac{2}{\beta_n R^2}\sin^2(R\beta_n)-\frac{1}{R}\sin(2R\beta_n)\right)\right]\right\} \tag{39}$$

4.2.3 Results

With several mathematical and physical models proposed for the spherical plastic tracer particles in a flow medium presented, the results are now shown. Each equation was evaluated numerically using a combination of Matlab™ and MathCad™ software (see Appendix A for listing of Matlab™ source code). The summation was taken from n = 1 to 1000, which will be shown in following sections to be extremely accurate.

Since the mathematical nature of the equations cause them to approach the final steady state value asymptotically, the exact time to reach equilibrium cannot be implicitly solved for. Instead, a nominal threshold value is chosen based on engineering judgement.

For the present purposes, a value of $\Theta = 0.99$ is chosen. Physically, this means that the temperature has reached 99% of it's final steady state value (or rather, 99% of the change from its initial to its final steady state value). If we then determine the time at which this occurs and do so for a range of particle sizes, we arrive at a relationship between particle size and critical time response as it shall be called (t_{crit}). This plot is shown in ***Figure 7***. Each Equation (11), (19), (31), and (39) was solved for the critical time over a range of particle diameters.. The critical time was determined by using a secant root finding method.

As Figure 7 shows, the time response for modest size particles such as in the current investigation (50-70 μm) is on the order of 2-5 ms.

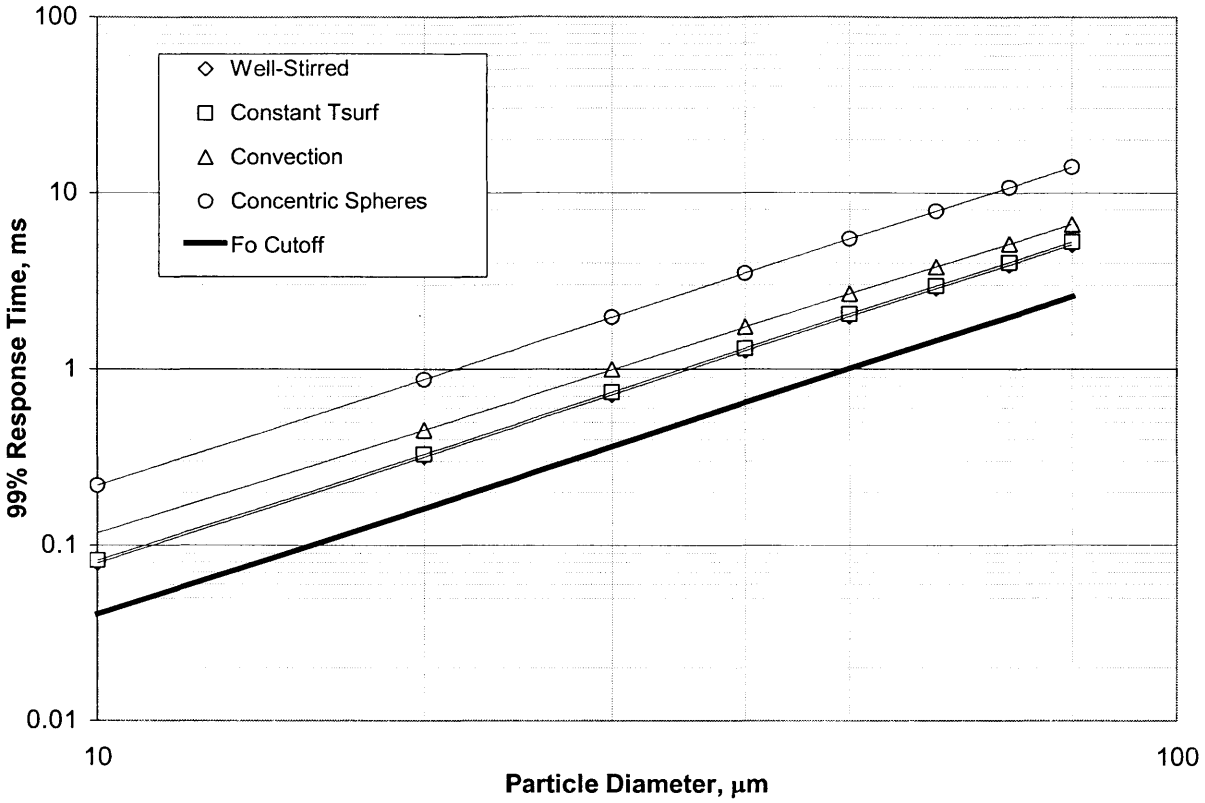

Figure 7 *- Particle Thermal Response Time.*

4.2.4 Discussion and Conclusions

Detailed analysis and explanation has been presented for several different approaches to modeling the spherical PIT tracer particles for thermal response time. Commentary is presented in the body of the preceding sections, and is summarized here. The convection solution is not deemed to be appropriate, for convection is predicated on a relative motion with the surrounding fluid. Argument is made that PIV is based on the fact that the particles move with the fluid (in the immediate vicinity), and therefore there is no relative motion with the fluid in the region of interest here. The constant surface temperature condition also most likely does not apply. The physical interpretation again is of a very high convection environment. The concentric sphere method is not a good physical model, as the material surrounding the particle is in reality a fluid and not a solid. Also, the outer radius R_2 is

arbitrarily determined. Putting this radius at larger and larger values continually increases the response time, as there is a larger resistance through he outer shell (i.e., gradients).

The well-stirred fluid approach is the one that makes the most sense physically. It is based on a simple energy balance of the particle and surrounding fluid. The mass of surrounding fluid can be increased, but the solution time will stop changing as this mass approaches an infinite bath. This occurs at relatively small radii, on the order of 2-5 times that of the particle itself. This is the method that is used for the remainder of the analysis, and the one that should be used for evaluating the PIT particles henceforth.

4.3 One Term Series Approximation

Regardless of the assumed boundary and initial conditions imposed on the spherical tracer particles, the mathematical solution always takes the form of an infinite series summation, as evidenced by Equations (11), (19), (31), and (39). However, these full summations are only necessary when the initial stages of transient heat transfer are involved. Heisler [14] shows that only a single term of the infinite series is sufficient for a dimensionless time, t*, greater than 0.2. Here, t* (also called the Fourier Number, Fo) is defined as

$$t^* = Fo = \frac{\alpha t}{r_o^2} = \frac{4\alpha t}{d^2}. \tag{40}$$

.

Solving for time t we obtain,

$$t = \frac{t^* \cdot d^2}{4\alpha} \tag{41}$$

This time t sets a lower bound for the applicable range for the one-term series approximation. For a given particle size (d), a response time can be calculated using one of the four methods and equations outlined above (for a given Θ). If the time calculated for a this Θ is smaller than the threshold time dictated by Equation (41), than the one-term series approximation is not valid. Greater than this threshold, and the one-term series can be utilized with little to no loss in accuracy. Figure 7 plots Equation (41), and shows that for any of the four modeling methods, the 99% response time is well above the threshold. Therefore, Equation (39) can be evaluated for only n=1 (first term).

The rationale behind choosing the 99% response time to investigate is based on the following supposition. A reasonable temperature range that is encountered in this study is approx. 25°C. In the case that a particle undergoes a step change of this amount the particle must be greater than 96% of the way to it's final state to be within less than 1°C. So for the current analysis a value for Θ of 0.01 (99% response time) is used.

The one-term series approximation is made not only to aid in computational efficiency and speed, but also to enable the solution to be explicitly solvable for time *t*. This expression for time is utilized in the following sections concerning particle size distribution.

The solution for the particle thermal response is now abbreviated using the 1-term series. For n = 1,

$$\Theta(t)_{AVG} = 1 - (\varepsilon + 1) \cdot A_1 \cdot e^{-\alpha\beta_1 t} \tag{42}$$

where A_1 is defined by

$$A_1 = \frac{1}{\beta_1} \cdot \frac{\varepsilon^2 (R\beta_1)^4 + 3 \cdot (2\varepsilon + 3) \cdot (R\beta_1)^2 + 9}{\varepsilon^2 (R\beta_1)^4 + 9 \cdot (\varepsilon + 1) \cdot (R\beta_1)^2} \cdot \left(\frac{2}{\beta_1 R^2} \sin^2(R\beta_1) - \frac{1}{R} \sin(2R\beta_1) \right) \tag{43}$$

4.3.1 Size Distribution Effect on Time Response

Like PIV, PIT analysis divides the image into interrogation regions, and works with averaging type algorithms to arrive at temperature. It is appropriate therefore to derive an average time response value for a sub region, based on an assumed particle distribution. To do this, Equation (39) must be solved explicitly for time. The one-term approximation derived in Equation (42) enables this analysis. This result is,

$$t(\theta, d) = -\frac{1}{\alpha\beta_1} \cdot \ln\left(\frac{1 - \Theta}{(\varepsilon + 1) \cdot A_1} \right) \tag{44}$$

where A_1 is given in Equation (43).

A certain size distribution of particles is assumed within a given image region. A Gaussian size distribution is used here to illustrate size distribution effects. A Gaussian distribution, with mean value of *m* and variation (standard deviation) *s* takes the form

$$G(d) = \frac{1}{s\sqrt{2\pi}} e^{\frac{-(d-m)^2}{2s^2}} . \tag{45}$$

Figure 7 illustrated the time response of individual particles of size d; smaller particles react faster than larger ones. As particle fluorescence is a function of volume, it is appropriate to calculate an average response time by weighting the individual particle time by its relative volume contribution to the population, given by Equation (45) and the volume, *V*. This weighting is accomplished by taking the integral over a given range of the product of population density and time, and dividing by the overall population density. That is,

$$t_{AVG} = \frac{\int_{d_1}^{d_2} [t(d) \cdot G(d) \cdot V(d)] dd}{\int_{d_1}^{d_2} [G(d) \cdot V(d)] dd} \tag{46}$$

Since the bounds for the range, d_1 and d_2, can be logically given as a function of the mean and standard deviation, the bulk average time is only a function of *m* and *s*. As such, the equation may be looked at in terms of the relative variation to the mean, or *s/m*. In addition, a good measure of the necessity of including the size distribution effect on the response time is given by examining the volume weighted average time to the normal response time for a particle of size *m*. Figure 8 shows this relationship.

Figure 8 shows that for a distribution where there is very little deviation from the mean value (i.e., *s* is small), the volume distribution weighted time approaches that of the equivalent single particle response time value for a particle of size *m*. However, for a relatively large particle distribution spread (*s* large → *s/m* large), the difference from a single particle time is less than becomes increasingly large. Indeed, as Figure 8 shows this relationship is exponential over the first 10-20% of *s/m*, and shallows out above this.

The end result is this: if a relatively small the particle distribution variation is assumed, the temporal threshold PIT validity is made simply by using the time response calculated for a particle of mean size *m*, given *by* Equation (42). If a relatively large variation is assumed (or known), then care should be taken and a reasonable threshold should be calculated using Equation (46).

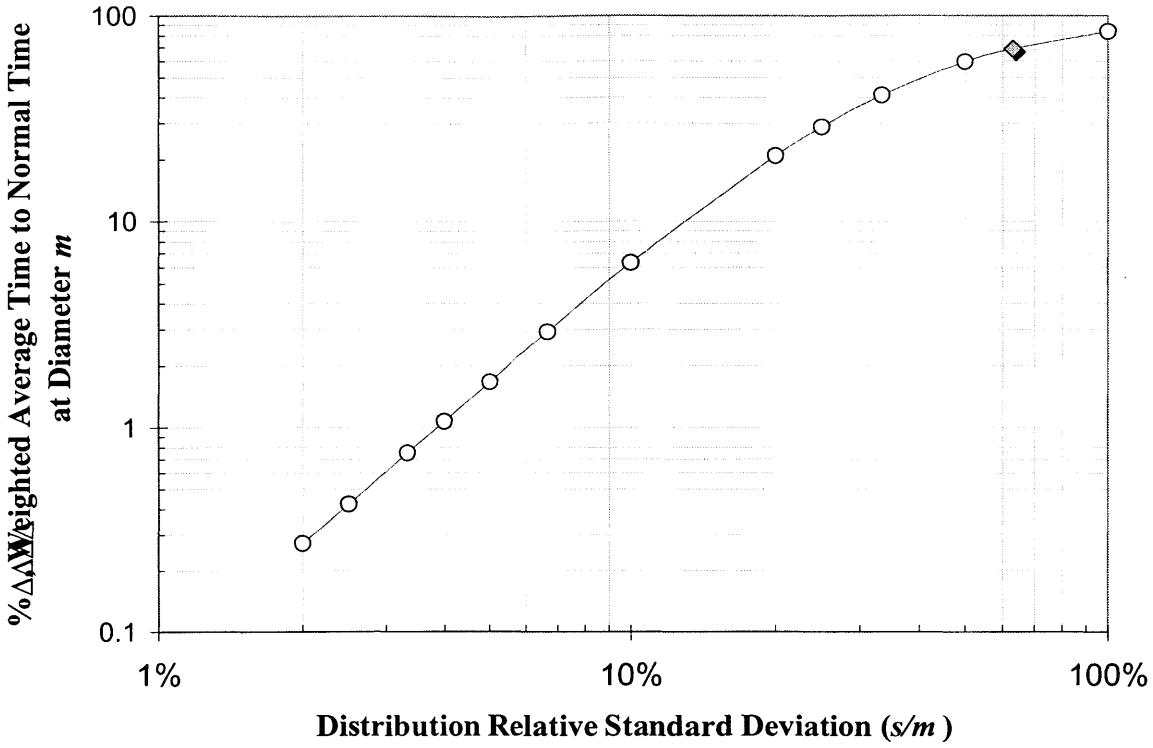

Figure 8 - Distribution Effect on Time Response

Thermal response may be an important factor by two scenarios. First, changes in the flow field may be extremely fast and one wishes to detect the temperature changes occurring in a time on the order of the laser pulse duration. In this instance, the time response outlined above should be calculated and monitored, as there is a potential risk of misinterpretation of the results. However, if it is desired to track the time evolution of temperature changes or gradients, then subsequent frames from a typical camera capture sequence are typically analyzed. Typical high-speed CCD imaging cameras used for PIV analysis have frame rates on the order of 30-100 fps. This translates to between 10 and 33 ms from frame to frame. This is ample time for even the large, wide variation particle distributions (per above) to reach steady state.

Chapter 5 - Image Analysis

5.1 Intensity Averaging Techniques

The idea behind DELIF is that the ratio of fluorescence intensity of each dye at a given point in the flow is calibrated to temperature based on the emission characteristics of both dyes. However, since particles used here are discretely distributed throughout the flow-field it is necessary to break the entire image into sub-regions, and perform an averaging technique over the region. An average intensity will capture the discrete particles in the region.

This sub-region averaging technique is similar to that used in PIV analysis. The entire image is divided into multiple *sub-regions* or *interrogation windows*. Each window is then analyzed by calculating the average particle fluorescence intensity. Depending upon the window size and particle seeding density, there may be large differences in the number of actual particles within the region. In addition, there is often 'background noise' associated with an image. Variations in laser light intensity, reflection of laser light, and impurities in the fluid medium can create light intensity values that do *not* represent actual particles. It is the nature of PIV type images to be bimodal, having light particles on a dark background.

The goal of each method is to obtain the true value of the average particle intensity in each sub-region, minimizing the impact of background noise. The straight mean method takes the mathematical average of all pixels in the sub-region. Intensity threshold methods only include pixel intensities *above* some value in the new region average. The sub-region mean can be used, as well as an arbitrary value, for the cut-off. Another threshold method is *gradient* clipping. In this case, the gradient of the pixel intensity is calculated, and a threshold formed based on the results. Since the gradient method scans through each row and column of the input image matrix, local areas of dark (or bright) pixel intensity are not included, and only the particles (with high intensity gradients) are chosen for inclusion into the mean.

5.1.1 *Strait Mean Technique*

As described above, the strait mean technique simply takes the mathematical average of all pixel intensity values within the interrogation window. The method is computationally efficient, as it only scans through the sub-region matrix once. For an arbitrary interrogation window (i, j), of size *m* x *m* pixels, this average intensity can be expressed by Equation (47).

$$\bar{I}_{i,j}^{M} = \frac{\sum_{a=1}^{m}\sum_{b=1}^{m} I(a,b)}{m^2} \tag{47}$$

While this approach is simple to implement, it does nothing to address the issue of potential (and probable) background noise in the image. Indeed, only for perfect images (i.e., perfectly black background, only fluorescing particles register any pixel intensity) will this method produce meaningful results.

A similar approach would be to use the sub-region median value as representative of the population. However, even for heavily seeded flows, less than 50% of the pixels in a given region represent intensity values from particles. Therefore, a median would fall within the background noise.

Figure 9 shows a typical 64 x 64 pixel interrogation region from a PIT image.

5.1.2 *Thresholding Technique*

A useful approach to obtaining a meaningful average intensity is based on methodically clipping the sub-region to eliminate from the average pixels that probably do not represent particles. The mathematical equation is very similar to Equation (47), except that *I(a,b)* is only included in the summation (and total count) if it is above a certain value. This value can be obtained in several ways. The two methods investigated here are based on the mean of the entire sub-region, and on the gradient of pixel intensity.

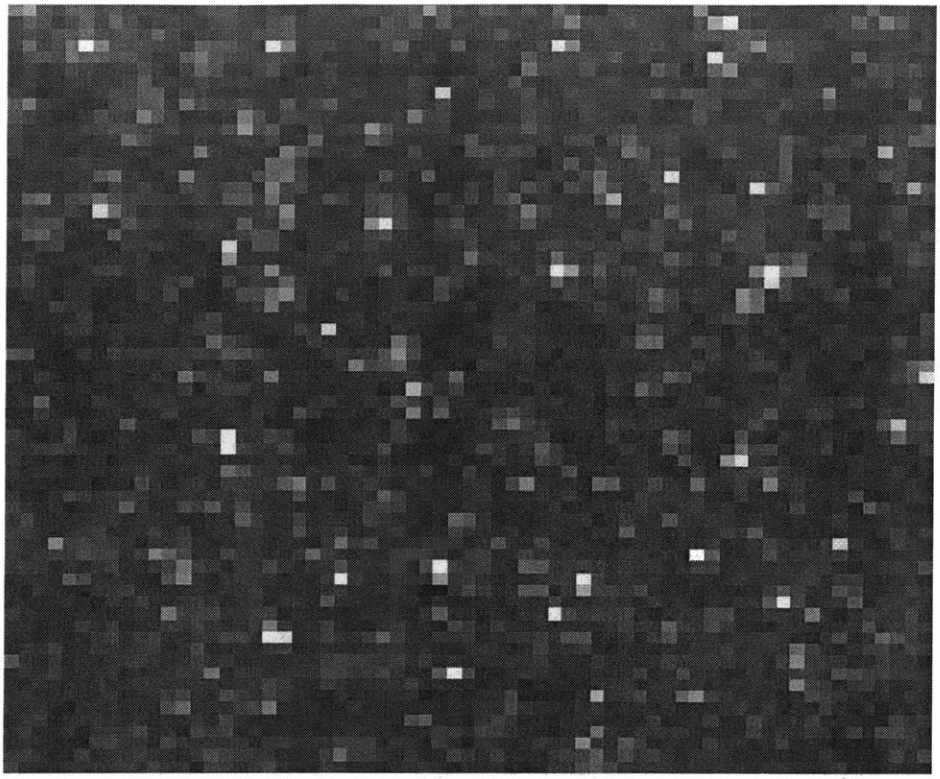

Figure 9 *- Typical 64 x 64 pixel region of a PIT Image.*

5.1.2.1 Mean Thresholding

As its name implies, this method uses the strait mean value for the entire sub-region, as calculated in Section 5.1.1, to clip the image. Only values above the original strait mean are included in the 'new' average intensity value for the region. This method can be modified as well, using the strait mean plus or minus some multiple of the standard deviation for example. This is similar in concept to an intensity distribution curve approach reported by Hart [15], where the threshold is chosen to correspond to a certain slope on the said curve. Imprecision in the current approach is not of great concern since as Hart et al. points out, the strongly bimodal nature of PIV images minimizes the criticality of the precise threshold level. Figure 10 shows the image region of Figure 9 after mean thresholding.

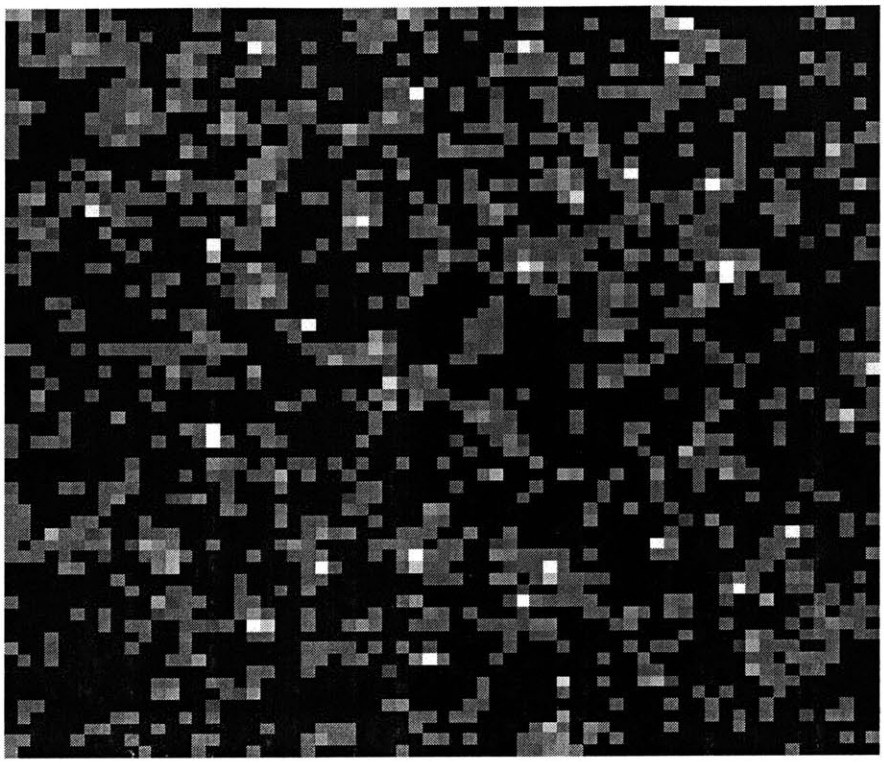

Figure 10 *- Sample 64x64 pixel image from Figure 5 after mean threshold clipping*

5.1.2.2 Gradient Threshold Method

As mentioned, threshold techniques can also be performed based on the gradient of the intensity. This is often a desirable method for the bimodal images in PIT analysis. It is identical in concept to the mean threshold, where only pixel values above a certain level are retained, except that the threshold level is established based on pixel gradients. For computational efficiency, the gradient can be approximated by

$$|\nabla I| \cong \left|\frac{\partial I}{\partial x}\right| + \left|\frac{\partial I}{\partial y}\right| \tag{48}$$

which, to a first order approximation, is calculated by,

$$|\nabla I| \cong \left|I_{(i+1,j)} - I_{(i,j)}\right| + \left|I_{(i,j+1)} - I_{(i,j)}\right| \tag{49}$$

As in the other method, a threshold value is established, this time based on the mean gradient, or more accurately by some selection of a slope on the cumulative gradient magnitude curve. In the current study, the cutoff value was chosen based on the gradient distribution. The statistical average of the pixel absolute gradient was calculated, as was the standard deviation (variation from the mean). The cutoff value chosen was the mean plus two (2) standard deviations. Figure 11 shows a contour plot of the absolute intensity gradient calculated from the original region of Figure 9.

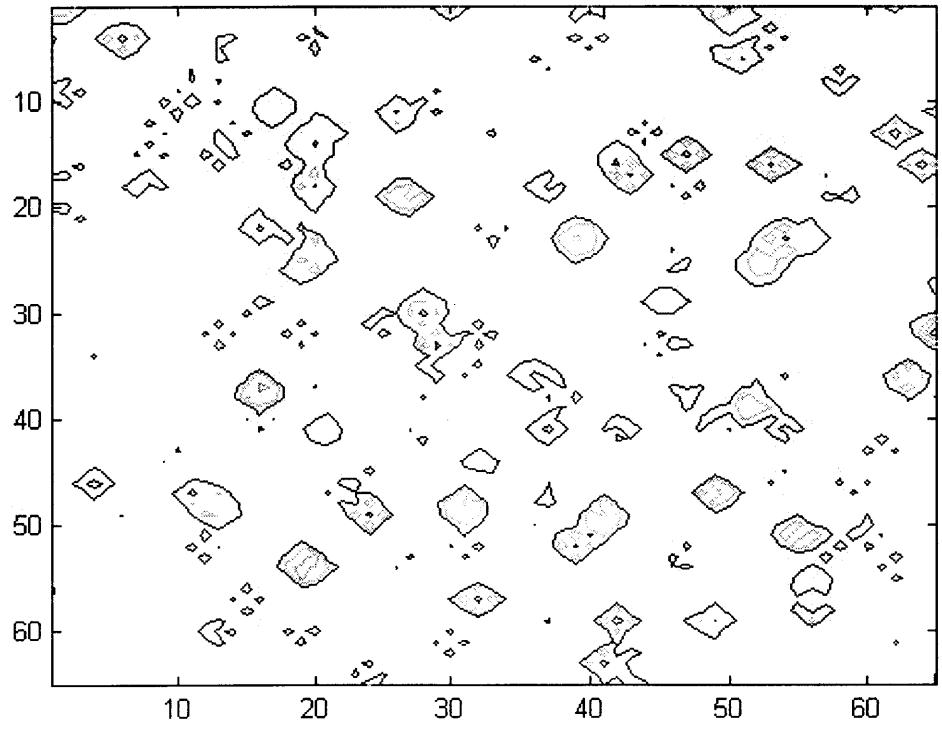

Figure 11 *- Pixel Intensity Gradient contour plot, from the image in Figure 9.*

Using the gradient information obtained and plotted in Figure 11, a threshold value is determined and the image clipped. Figure 12 shows the image after gradient clipping. The remaining pixels are used for intensity averaging.

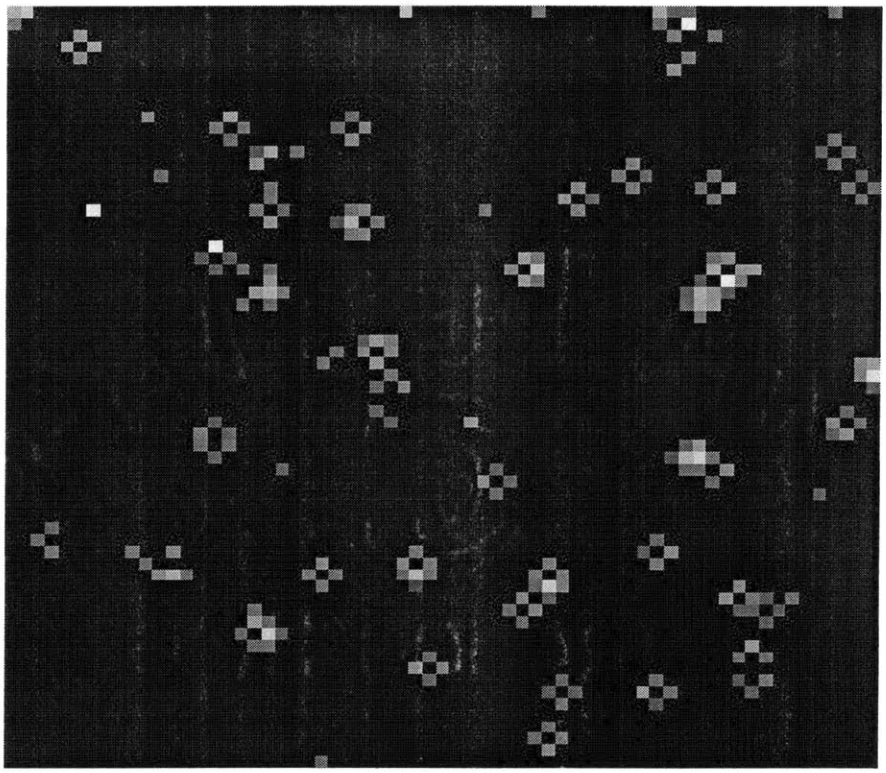

Figure 12 *- Sample image from Figure 5 after Gradient Threshold Method*

An interesting phenomenon occurs often with gradient threshold methods, referred to as the *top-hat* effect. The ideal pixel intensity profile is assumed Gaussian in nature, as illustrated in Figure 13. Along the edges of the profile, the gradient is somewhat shallow. This also occurs near the top of the profile, near the peak intensity. In both of these regions, it is possible for the pixels to be eliminated due to the relatively shallow gradient. For PIV analysis, it has been shown that this effect has minimal bearing on the ability to correlate the images for velocity. This is presumably also the case for DELIF, where the ratio of image intensities will negate the fact that some potentially important pixel intensities have been eliminated from the average. Figure 14(a) plots the intensity along a central symmetry line from Figure 13. Figure 14(b) shows the gradient of the intensity, with a horizontal line showing the value chosen for a cutoff (the mean pixel gradient in this case). The resultant profile after clipping below a certain gradient level is shown in Figure 15. This example is shown with very fine detail (i.e., a fine mesh) to illustrate the concept. In reality, particle

images often occupy a diameter of only about 3-4 pixels. This phenomenon still occurs however.

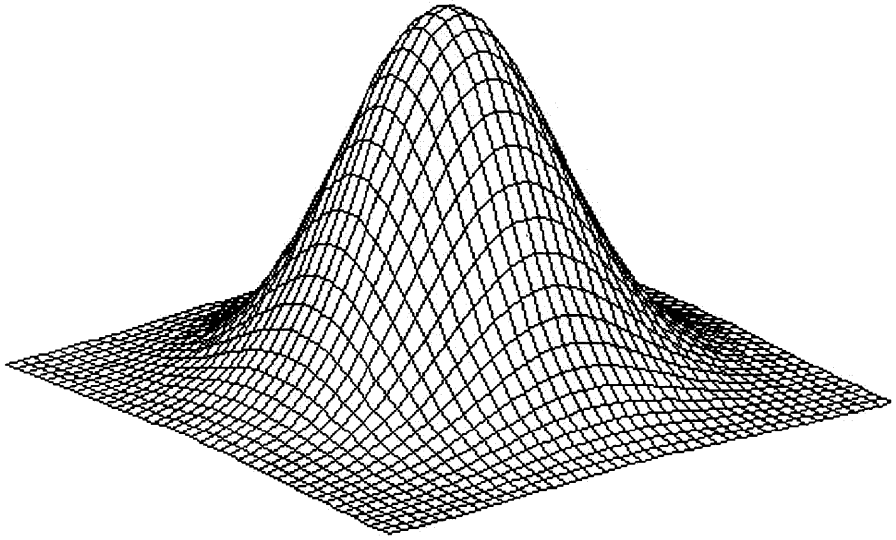

***Figure 13** - Representation of Gaussian Particle Pixel Intensity Profile*

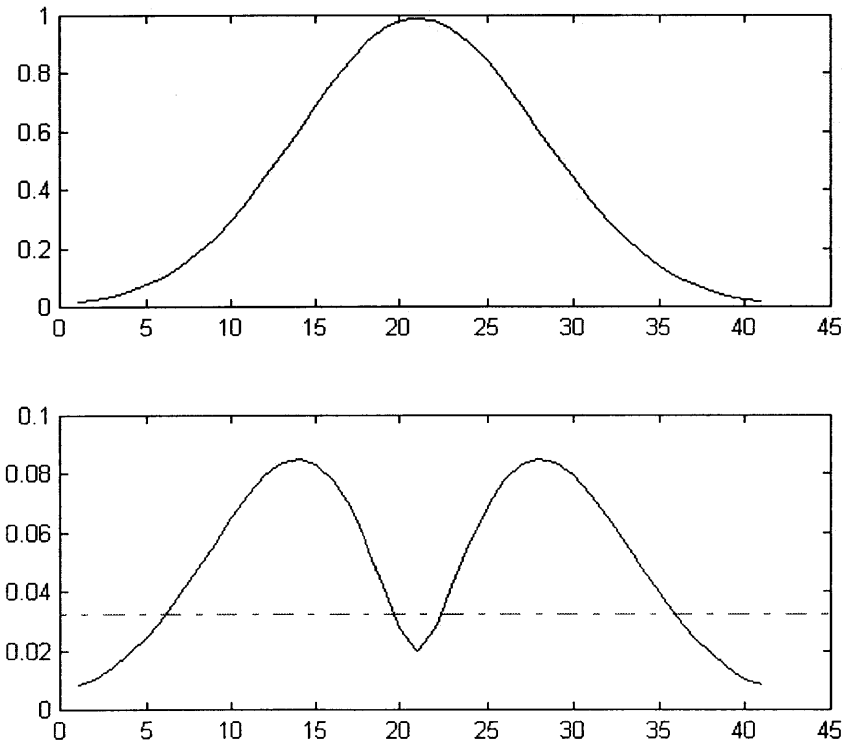

***Figure 14(a) (top)** shows Gaussian intensity distribution along symmetry line.*
***Figure 14(b) (bottom)** shows the calculated gradient with the clipping value.*

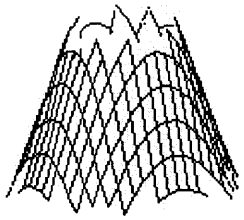

Figure 15 *- Gaussian intensity profile after gradient clipping.*

Mathematical proof of the validity of utilizing the gradient clipping method is neither necessary nor appropriate. The gradient is used to determine which pixels in the sub-region will be used for the average and which will not. The intensity gradient itself is not being used for the averaging.

Another effect that can be seen in Figure 12 by the many black spots surrounded by brighter pixels is elimination due to pixel saturation. These 'holes' most likely represent relatively bright pixels eliminated due to saturation. If the fluorescence intensity is great enough, or the imaging system not sensitive enough, the CCD chip at that location may reach its saturation point and register the maximum value. It is usually assumed that a pixel in this state may in fact be brighter than it's recorded maximum value, and thus is invalid. For the images in the present investigation, a standard 8-bit black-and-white CCD camera was used. From this, we obtain 2^8, or 256 gray-scale levels. For each of these averaging techniques, saturated pixels were eliminated.

5.1.3 Evaluation of Averaging Techniques

The previous section detailed the theory behind each of the techniques of sub-region intensity averaging considered in this study. To evaluate each method, a synthetic PIT image pair was created and given a known "temperature" profile (i.e., region of one image given

decreased pixel intensity to simulate decreased intensity of one fluorescent dye with increased temperature). This image pair is shown in Figure 16. The image pair was then analyzed using each method, for the same interrogation window size and overlap. Figure 19 shows this evaluation of the different methods for a 32 x 32 pixel sub-region with 50% overlap.

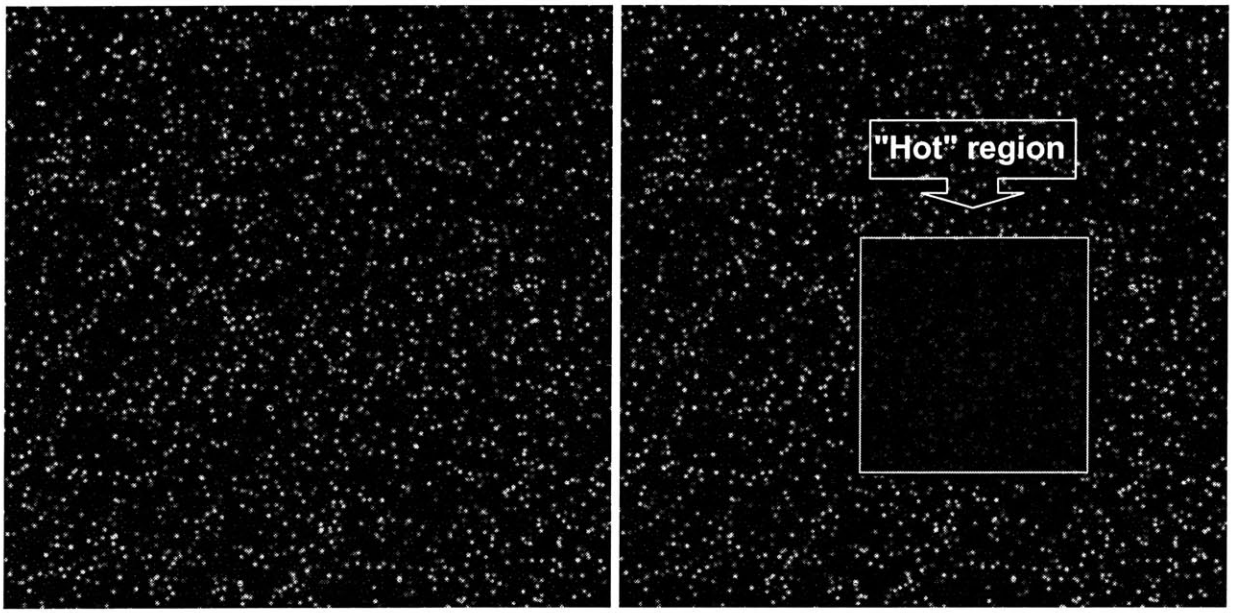

(a) *(b)*

***Figure 16** - Synthetic PIT Image Pair. Left image (a) and right image(B) are identical, except (b) has region of reduced intensity to simulate "hot" temperature.*

Figure 16 shows the sample PIT image pair used for this evaluation. The images are identical except that the image *(b)* has a square region of reduced pixel intensity (80% in this example), intended to simulate the reduced fluorescence of the Rhodamine B dye at elevated temperatures.

The basis for evalutation of the different techniques was to determine how accurately and precisely each method predicts the know distribution. This distribution is a step change in pixel intensity, covering an area as depicted in Figure 16. An example contour plot is shown in Figure 17, the result of 32 x 32 pixel subregions with 50% overlap using the strait mean method. Qualitatively, the structure of the stepped intensity depression is easily seen. Since the images are identical, the ratio is unity except for the depressed region. The intensity

mean method. Qualitatively, the structure of the stepped intensity depression is easily seen. Since the images are identical, the ratio is unity except for the depressed region. The intensity is stepped down by 80% (i.e. ratio is 0.2) inside the simulated hot region. This can be seen in the figure. The dashed lines superimposed on the contour represent the known center of the depressed region, and the white square represents it's location and extent. It is seen that due to the discrete particles, averaging method, window size and overlap, the contours are ragged near the edges, and offset from the exact center of the know profile.

To assess the methods *quantitatively*, a slice was taken along the centerline of the distribution, and the intensity averaging results compared to the predicted (i.e., known) intensity at that location. An example of this is shown in Figure 18.

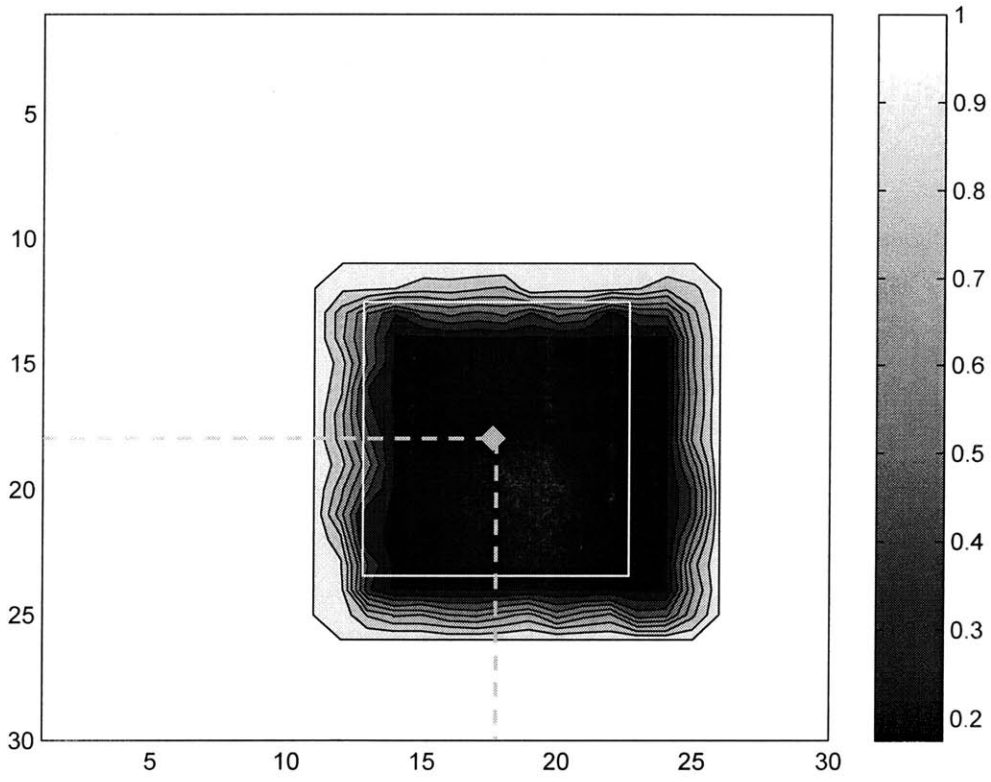

Figure 17 - Example PIT Image Analysis. X- and Y- axes are indices. Ratio contour legend is to the right.

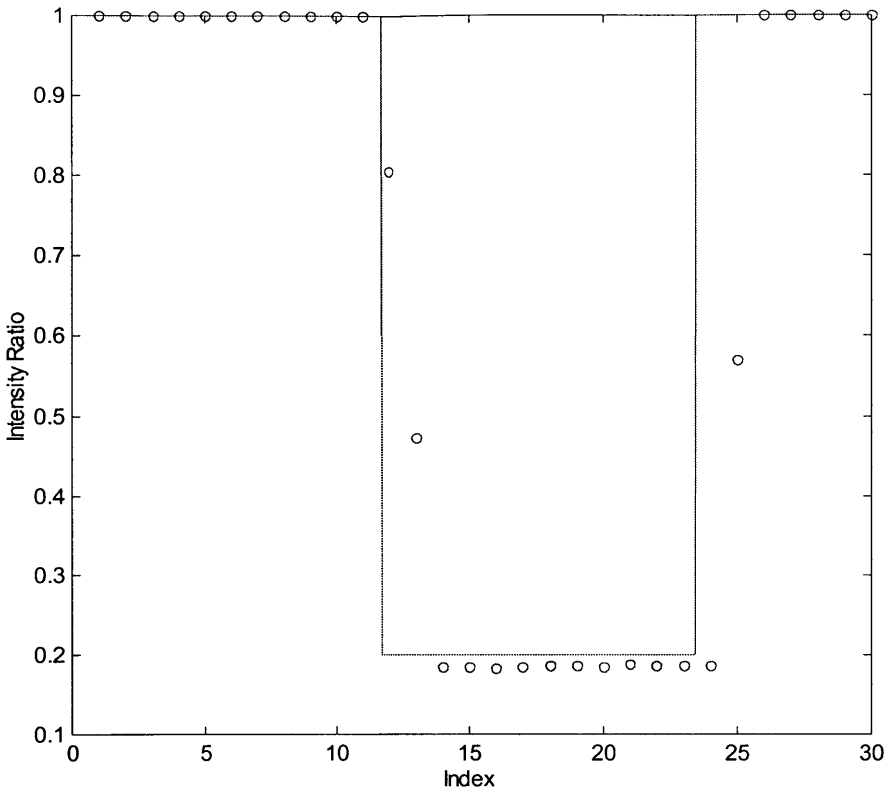

Figure 18 *- Example comparison of imposed step distribution along symmetry plane (solid line) and calculated average intensity ratio (circles) using strait mean analysis technique.*

For each sub-region the difference between the computed intensity average ratio and the known profile was calculated. This was done for each of the three methods, and the results plotted in Figure 19. The analysis was done using 32 x 32 pixel sub regions with 50% overlap. The data shows that although in theory it would appear the gradient clipping method would have better results, in fact all methods are fairly good at approximating the known answer. However, it should be noted again that the images used were synthetic, with little background noise. As background intensity noise is increased, the gradient method is most likely to handle the analysis better than the other methods.

It is recommended based on the preceding exercise that the gradient level image clipping method be used for PIT analysis.

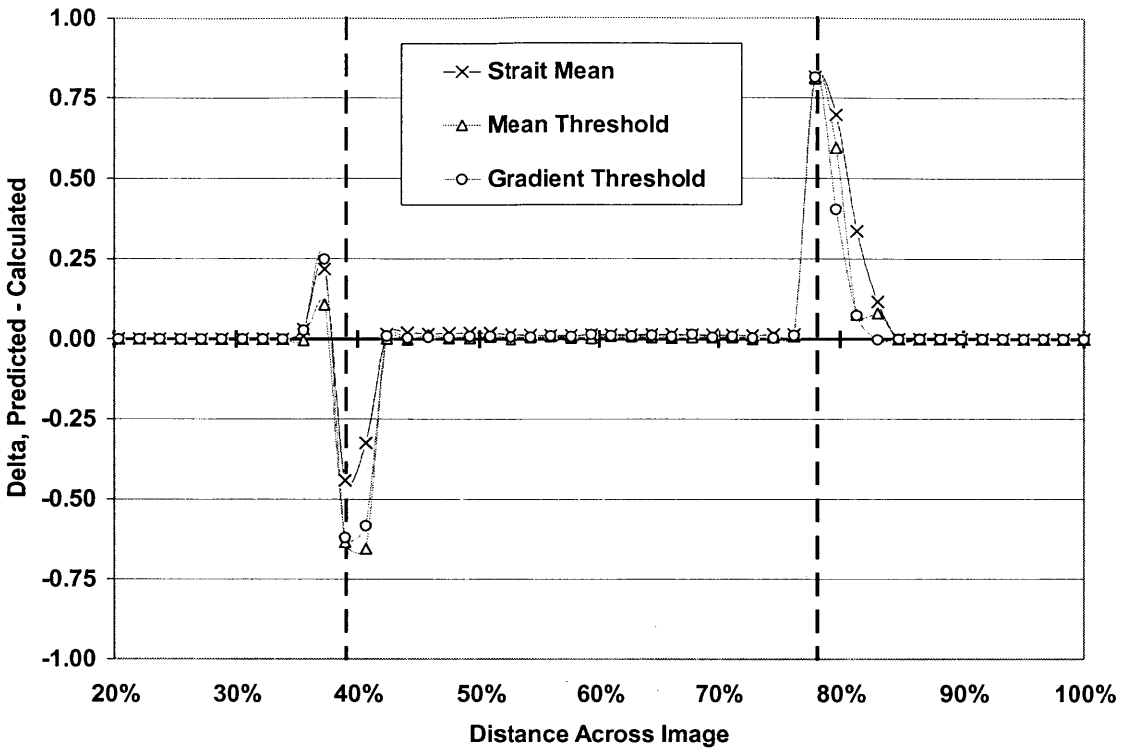

***Figure 19** - Evaluation of Interrogation Region Average Intensity Methods*

5.2 Interrogation Window Optimization

While determining the best type of sub-region analysis method as done in the previous section, the question arises as to how best to define a sub-region to begin with. The two largest aspects of this question, and those investigated here, are what is the best/optimal sub-region size (window size in pixels), and how much, if any, window overlap should there be. These issues are addressed in the following sections.

5.2.1 Window Overlap

Conventional PIV analysis algorithms typically utilize a 50% window region overlap for correlation. For the statistical and error type of cross correlation calculations, this appears to be an optimal overlap, providing the most amount of information while keeping

computation time down. It agrees with sampling theory, and in general, if more than 50% overlap is used, it does not really add any new information to the system.

However, for the DELIF technique, it appears that window overlap has an impact, and that larger than 50% provides a better analysis. Where PIV is using the intensity information to statistically predict the probable average particle displacement, the DELIF is based on the fact that it can accurately calculate average particle fluorescence intensity, and use this value for directly relating to the fluid temperature. For the same synthetic image used in Section *5.1 Intensity Averaging Techniques* analysis was performed using varying amounts of window overlap. To minimize variation, a standard window size of 32 x 32 pixels was used. The same criteria as plotted for the method analysis was used. That is, the differences between the calculated image intensity ratio and that of the known distribution. The amount of window overlap was varied from 25% up to 95%, with the results plotted in Figure 20.

The data in Figure 20 shows that there is a definite correlation with window overlap. The greater the overlap amount, the more "smoothed-out" the resultant intensity ratio matrix (i.e., image) is, which inherently increases the resolution of the result. For a 512 x 512 pixel image as studied here, a 32 x 23 pixel interrogation window size with 50% overlap produces 30 sub-regions in the x- and y- direction. Alternatively, a 95% overlap produces nearly 300 sub-regions in each direction. As shown in Figure 20, the boundary at the intensity step decrease becomes more defined as the window overlap increases. However, as with most scientific and engineering situations, there is a tradeoff. In this case, computation time increases exponentially with greater window overlap. Figure 21 plots the normalized computational time (ratio to time required to compute 50% overlap). It is seen that up to about 80% window overlap, there is only a 2-3 fold increase in calculation time. However, moving to a 95% window overlap increases the time by a factor of 70. The 95% overlap does not provide a significant enough increase in accuracy (see Figure 20) to warrant this enormous increase in computation time. Calculations were performed on an IBM-compatible PC, with a 200-MHz AMD K-2 processing chip with on-board math co-processor and 64 Mb of RAM.

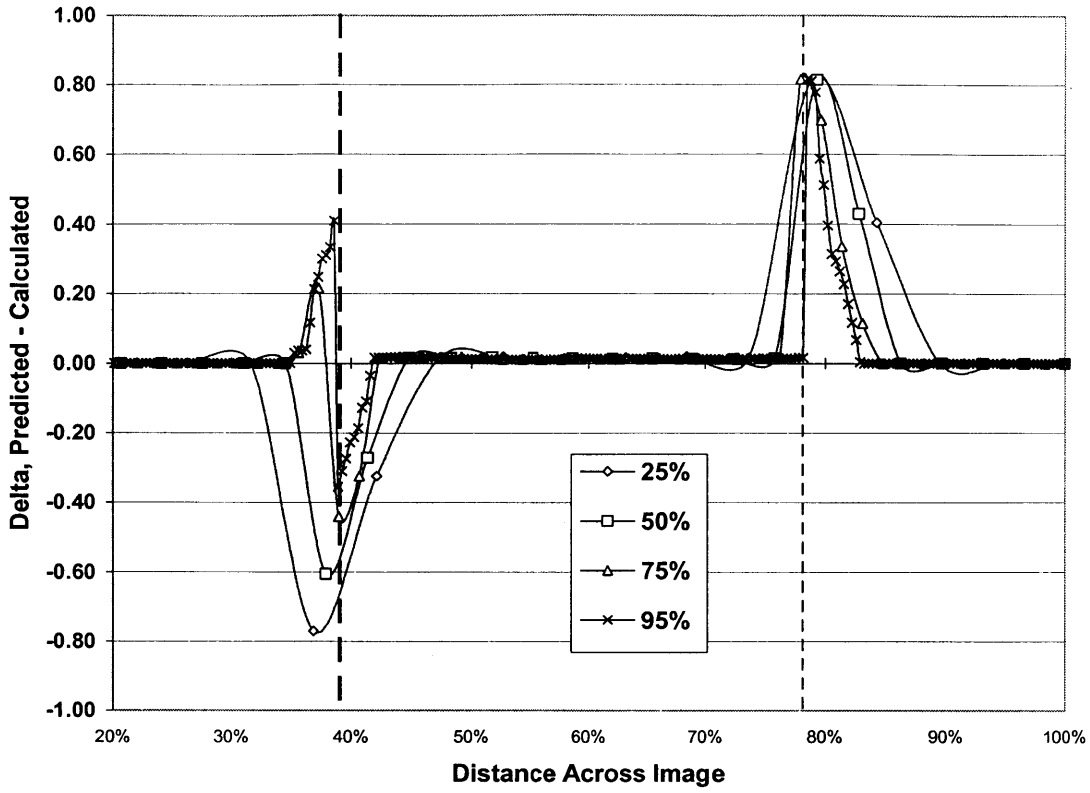

Figure 20 *- Window Overlap Study. X-axis is normalized distance across image. Y-axis is difference between calculated and actual value*

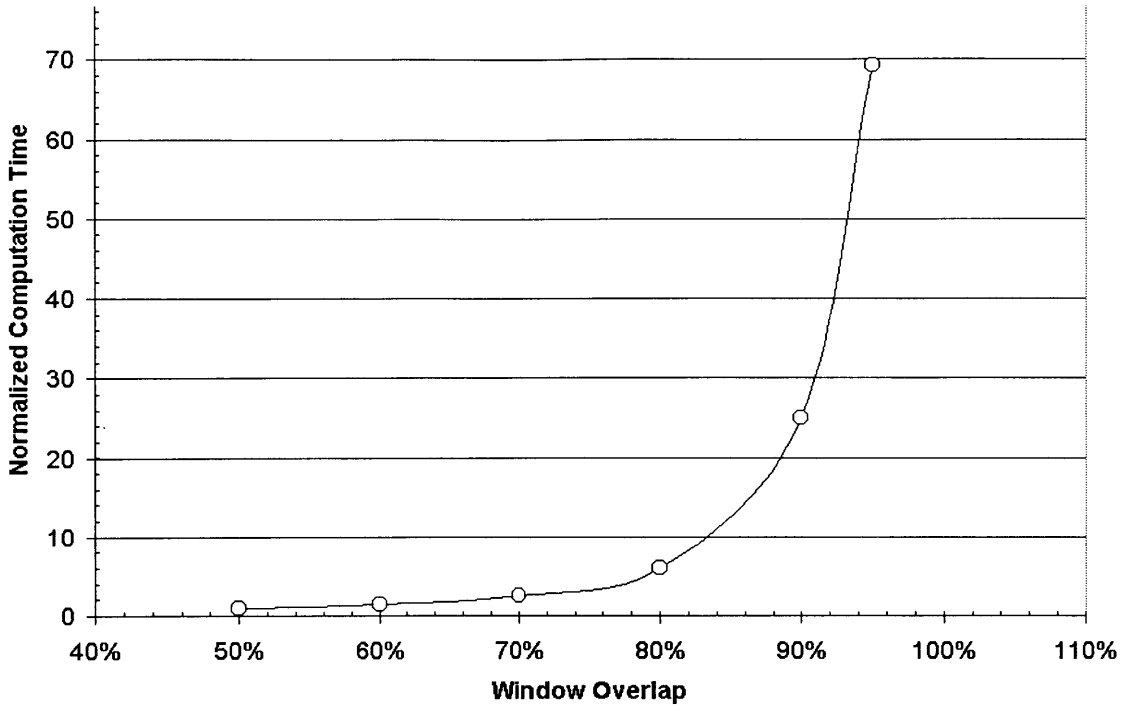

Figure 21 *- Window Overlap % vs. Computation Time*

5.2.2 Window Size and Seeding Density

To determine an appropriate window size to use for this analysis, synthetic images were again utilized. A 512 x 512 pixel image with a prescribed seeding density and average particle size is created. Starting from the center of the image, the intensity average of successively larger sub-regions are calculated. To normalize the result, the average is divided by the current window average intensity. Mathematically, this is expressed by

$$\Delta I_m = \frac{\left[\dfrac{\bar{I}m_i - \bar{I}m_{i-1}}{m_i - m_{i-1}}\right]}{\bar{I}m_i}, \tag{50}$$

In theory, the percent change in average intensity should decrease as the window size becomes larger. To obtain a larger sample of this process, several synthetic images were analyzed. Results for seeding density of 4000 particles/image are plotted in ***Figure 22***.

The figure shows that for this seeding density, the average sub-region intensity is changing by less than 5% for 32x32 pixel window size and less than 1% for 64x64 and greater. Also plotted in Figure 22 is the 'theoretical' relationship. While not exactly matching the data, it does show the overall trend and order of magnitude very well.

The theoretical relationship can be described as follows. It is noted that the theoretical changed as described discretely by Equation (50) can be expressed as

$$\Delta_{THEORY} = \frac{\partial I / \partial m}{I} = \frac{\dfrac{\partial (I_e \phi \varepsilon C V)}{\partial m}}{I_e \phi \varepsilon C V} \tag{51}$$

This assumes a first order backward-difference approximation to the derivative is being used in the synthetic image analysis. The definition for fluorescence intensity per Equation (1) has been substituted. Since the total particle volume V for that sub-region is the only variable dependant on window size *m*, the rest can come out of the derivative.

$$\Delta_{THEORY} = \frac{I_e \phi \varepsilon C \dfrac{\partial V}{\partial m}}{I_e \phi \varepsilon C V} = \frac{\dfrac{\partial V}{\partial m}}{V} \tag{52}$$

Now it is necessary to define the particle volume for a given sub-window size. First define a seeding density as

$$\rho_s = \frac{N}{512^2}. \tag{53}$$

Here, N is the number of particles prescribed during the program input that generates the synthetic images. The density units then are *particles/pixel*^{2}. This is an easy convention to use in the case of synthetic images. It could easily be translated into a true density or concentration by knowing what area the image occupies (512 pixels square = X square inches), and the thickness of the laser sheet. This would give a *particles/volume* unit.

For a given window size *m*, the window is *mxm*, or m^2 pixels. Assuming a uniform spatial distribution of particles, the total number of particles for any window size can then be calculated. This is

$$n = (m \times m) \cdot \rho_s = m^2 \cdot \rho_s .$$

(54)

The total number of particles in the subregion is equal to the total number of particles n times the distribution weighted average volume. This weighted average is based on a Gaussian distribution of particle size $G(d)$, as presented earlier.

$$f = \frac{\int_{d_1}^{d_2} [G(d) \cdot V(d)] dd}{\int_{d_1}^{d_2} [G(d)] dd} \tag{55}$$

The volume of particles then is

$$V = n \cdot f = m^2 \cdot \rho_s \cdot f \tag{56}$$

Substituting Equation (56) back into Equation (52),

$$\Delta_{THEORY} = \frac{\frac{\partial V}{\partial m}}{V} = \frac{\frac{dV}{dm}}{V} = \frac{\frac{d(m^2 \rho_s f)}{\partial m}}{m^2 \rho_s f} . \tag{57}$$

Performing the calculus,

$$\boxed{\Delta_{THEORY} = \frac{2m\rho_s f}{m^2 \rho_s f} = \frac{2}{m}} . \tag{58}$$

Equation (58) reveals a very simple theoretical relationship between the average intensity change and sub-region window size. This relationship closely matches that obtained in the synthetic image analysis as shown in Figure 22. Equation (58) also points out another fact that is *not* supported by the synthetic image data. Equation (58) says that relationship of the changing average intensity for progressively larger sub-region sizes is *independent of seeding density*. Figure 23 shows the same synthetic image technique for pictures where the seeding density was set to N=2000 (i.e., half the number of particles as in Figure 22). While the theoretical line of course does not move, the data does. Indeed, for lower seeding, the average window intensity continues to change from one window size to the next longer than the higher density. The reason for this difference most likely lies in the assumption of

uniform spatial distribution of particles used in the theoretical calculation. The program used to create the images uses a random number generator to place the N particles throughout the image. This random probably does not follow a uniform distribution pattern, and therefore causes an inconsistency with the theoretical calculation as presented and the actual results of image analysis.

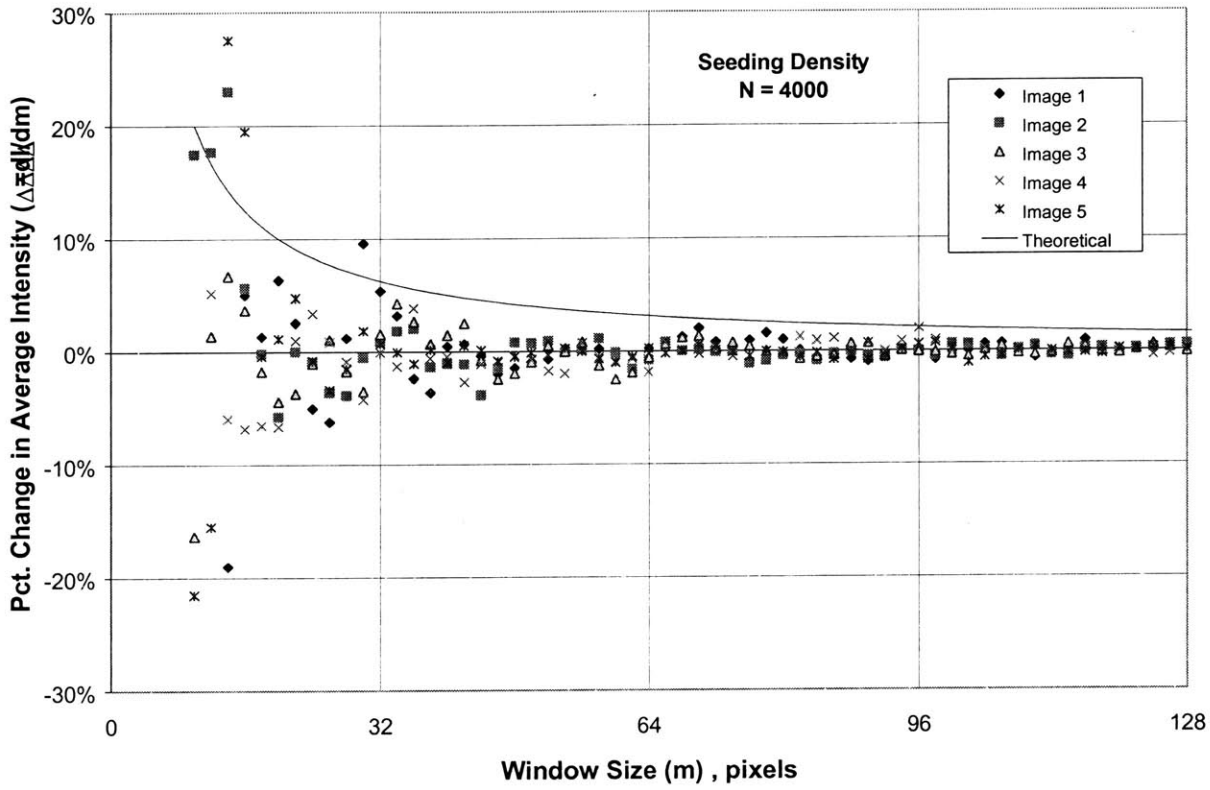

Figure 22 - Window Size Effects, N=4000

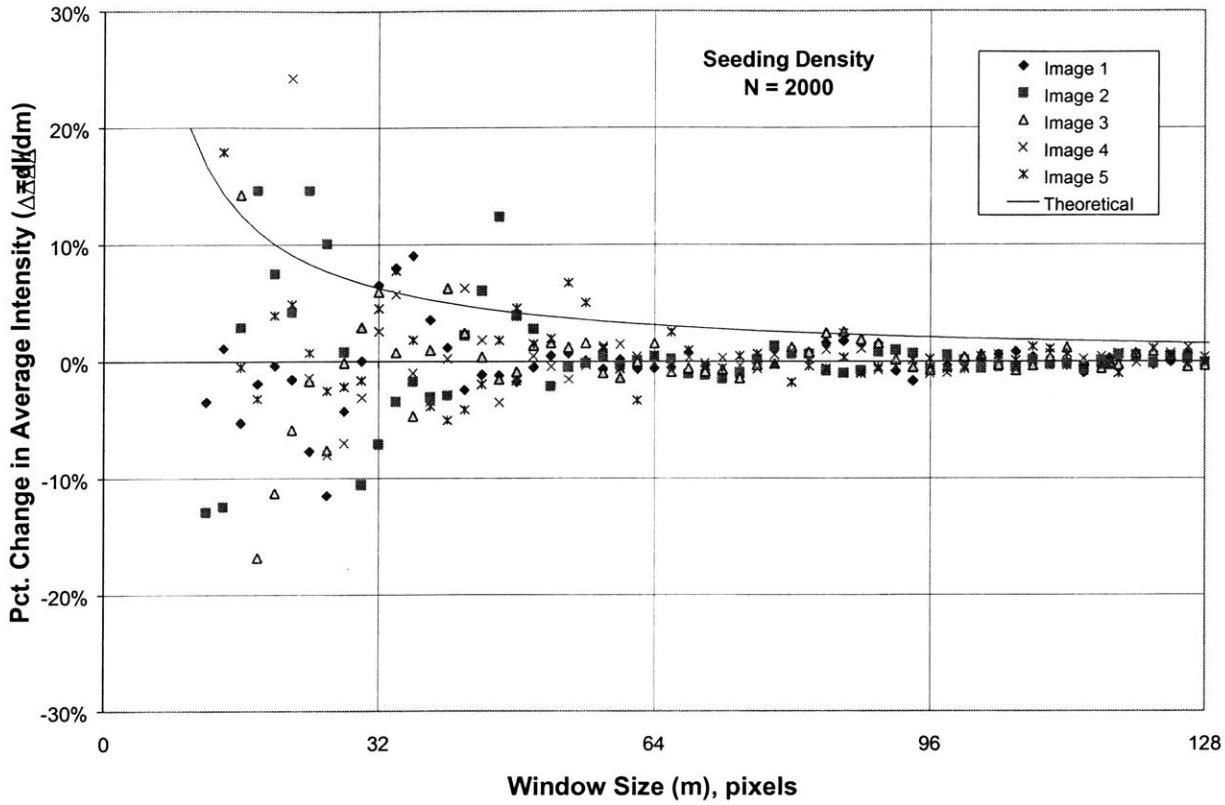

Figure 23 - Window Size Effects, N=2000

Even for the lower seeding density, less than 10% change is seen. By m=64, the change is less than 3%, very similar to the higher densities. However, there is a tradeoff in window size. For the type of intensity, average processing performed here, there is a skewing of results for larger window sizes. Processing the image is done in a logical progression across the image matrix, from left to right and top to bottom. Therefore, a larger window size will capture more pixels in the regions to the left and top, causing a skewing of the results. While an increased window overlap will help to minimize this effect due to its higher resolution results, we have already established that greater window overlap severely increases processing time. In addition, the increase in window size will also increase processing time. Therefore, an optimum size for practical purposes is either a 32x32 or 64x64 pixel sub-region. In the current analysis, a 32x32 pixel region was selected as most efficient.

5.3 Analysis Technique Conclusions

Based on the analysis of the preceding sections, it is determined that the PIT images should be processed using a 32x32 pixel sub-region with between 50% and 85% window overlap. The averaging technique used should be a gradient clipping method, with the threshold value based on either the mean of the absolute gradient, or that mean plus some standard deviation. The current analysis used mainly 32x32 pixel regions with 80% overlap and the gradient method.

Chapter 6 - Experimental Proof-of-Concept

After deriving the theoretical baseline for this technique and determining the appropriate image analysis method, it was necessary to prove this method by conducting a basic experiment. The experiment chosen needed to have the capability of producing sizeable temperature gradients. A cold water jet entering a hot tank of water was chosen for this simplicity and large gradient.

6.1 Setup

A rectangular tank (22.8 cm L x 15.2 cm W x 17.8 cm D) was filled with particle laden water. An electrical resistance foil heater mounted to the bottom of the tank controlled the water temperature through a resistance dial. Two type K open bead thermocouples were immersed in diametrically opposed positions in the tank to monitor and regulate tank temperature. Figure 24 shows a schematic of the experimental setup.

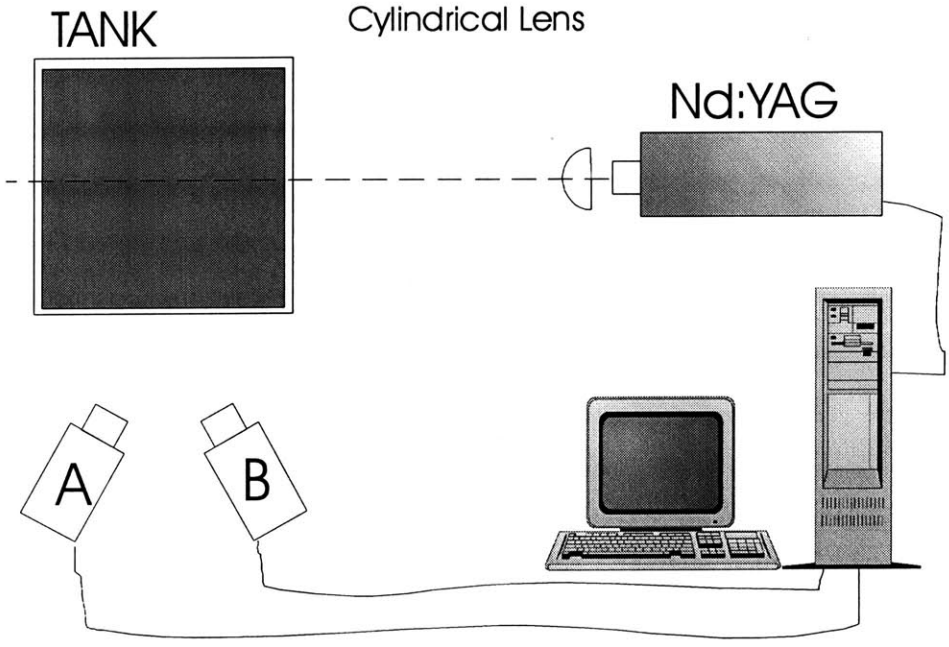

Figure 24 *- Schematic of Experimental Setup*

The receiving optics consisted of two TSI Inc. *PIVCAM™ 10-30* 1000 x 1016 pixel 8-bit CCD imaging cameras. These cameras are part of TSI's stereoscopic PIV system, capable of accurately determining not only the regular 2-D velocity vectors in a flow field, but the 3-D out-of-plane component as well. Hence the name 'stereoscopic'. A sample picture of these cameras, and the typical angle relationship is shown in Figure 26. The exact angle of the cameras in relation to each other is not very important, as TSI's calibration procedure removes the dependence upon the exact values. All that is important is that the angles, distances, etc remain consistent throughout the experiment(s). The arrangement of the cameras (object plane, lens, and image plane) is created such that the inherent loss of focus is minimized. Employing the Scheimpflug condition does this. This is illustrated in Figure 25. Here, plane A-A is the *object* or *illumination* plane (measurement plane), plane B-B is the image plane (where the CCD chip records the data), and C-C is the lens plane. To satisfy the Scheimpflug criteria, the planes must all intersect at the same point, noted by D here.

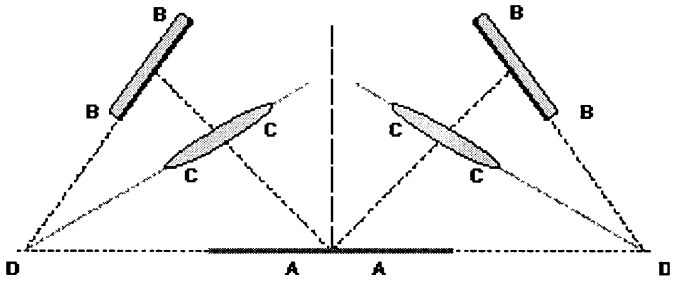

Figure 25 - Steroscopic Camera Schematic *illustrates the Scheimpflug criteria, where object plane, image plane and lens plane all meet at a single point.*

Both cameras were fitted with a 50 mm objective lens, which provided zoom, aperture, and precise focus capability. In addition, each camera utilized a narrow band-pass optical filter to transmit only light near the peak emission wavelength of each dye. The left camera (camera A) had a filter with λ_t=580 nm (CVI Lasers™, 580nm) to pass only light near the peak emission of the Rhodamine B. Likewise, the right camera had a filter with transmittance λ_t=630 nm (CVI Lasers™, 630nm) to pass emission of the Pyrromethene 650 dye. The optical filters have a full-band half-width (FBHW) of 4 nm.

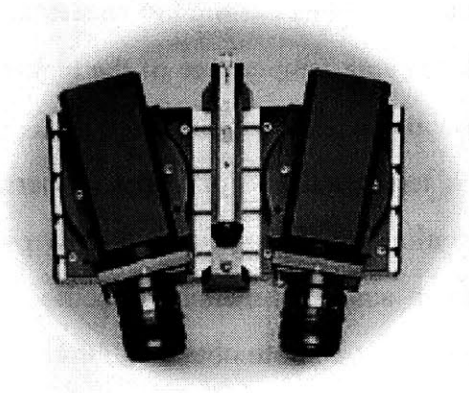

Figure 26 - TSI's PIVCAM™ 10-30 Stereoscopic PIV Camera System

Excitation of the particles was accomplished using a 50mJ/pulse frequency-doubled pulsed Nd:YAG laser (NewWave Lasers™), with a wavelength λ = 532 nm. The laser beam was expanded to a sheet using a cylindrical lens mounted within the laser head exit plane. The focal length and orientation of this lens could be adjusted to optimize the width of the laser sheet at a given distance (i.e., at the tank/image plane of interest).

The laser and both cameras were externally linked by a timing synchronizer (TSI Inc. *LASERPULSE*™ Model 610032). This in turn was connected to a PC data reduction computer running TSI's Insight software. Via the synchronizer, the software controlled both laser and camera timing.

6.2 Experimental Procedure

The experimentation was conducted with two goals. The first was to obtain sufficient data for an adequate temperature-intensity ratio correlation. The second goal was to capture images with definite and distinct temperature gradients, for analysis and proof that the PIT concept works. Based on previous experimental work, a temperature range from approximately 25°C-60°C was investigated.

To collect data to accomplish the first goal, the tank was slowly heated to different temperatures. At each temperature (9 temperatures ranging from 27°C to 62°C), a series of five (5) stereo image pairs were recorded. Tank heating was not stopped during the sequence. However, as the temperature rise in the tank was very slow (about 0.75°C/min), the bulk

temperature change would be negligible over the time necessary to capture the images (~ 300 ms $\rightarrow$ 0.004 °C). As noted, the bulk temperature of the tank was measured continuously by two thermocouples. Thermocouples placed on opposite sides and in opposite corners of the tank measured the bulk tank temperature. For every temperature, the two T/C's agreed to within 0.5°C . To avoid settling of the particles and to provide low level, background movement for PIV analysis, a small submersible electric propeller was placed near the bottom of the tank. Results of this attempt to obtain calibration data will be discussed later.

To obtain an image with a great temperature difference, as well as a distinct velocity field for the PIV analysis, a cold jet of water was fired into the tank of hot water. The jet was created using a funnel placed at the water line. Cold, particle-laden water was poured into the funnel, and it exited as a jet into the tank. The jet exit velocity is roughly calculated at 1.25 m/s. The tank water was at 60°C, and the cold jet was at 16°C.

For all images taken (both calibration and proof series), the following settings were used. The left camera (A) was fitted with the 580-nm filter (for Rhodamine B), using an *f*-stop of 4.0, focussed on the particles in the flow. The right camera (B) was fitted with the 630-nm filter (for Pyrromethene 650 emission), with an *f*-stop of 2.8. The laser and camera settings were all controlled through the software. The laser was set on High power, utilizing both Nd:YAG laser heads. Laser pulse repetition rate was at 15 Hz, with a 1000 μs pulse spacing and 0.25 ms pulse delay. The camera timing was set to run in frame straddling mode.

6.3 Results

Examples of the image results are shown here. Figure 27 shows an PIT image of the cold jet of water entering the hot tank. The picture shown is from the Rhodamine B filtered camera (580-nm).

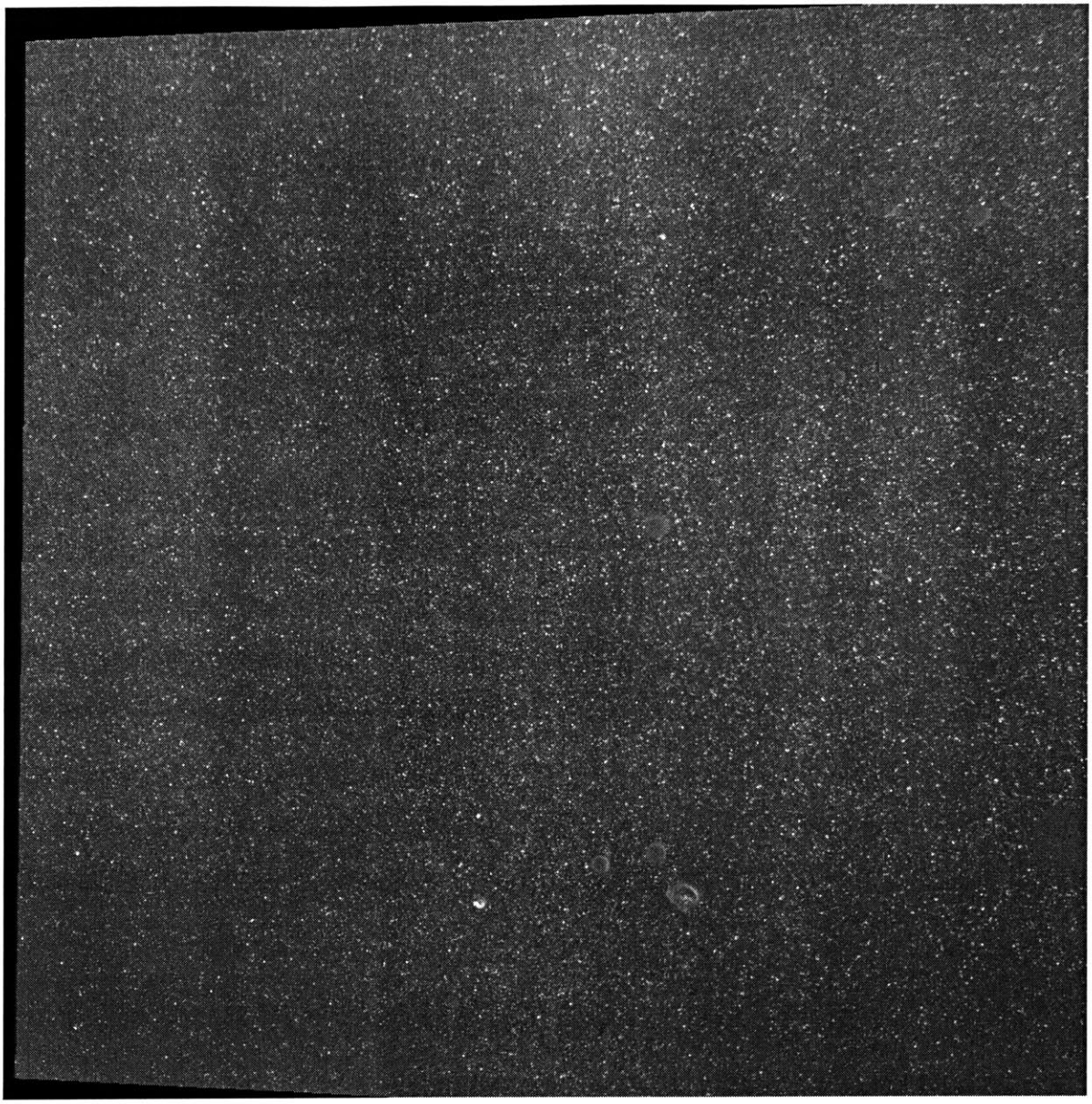

***Figure 27** - PIT Image of Cold Jet Entering Hot Tank, 580-nm filtered*

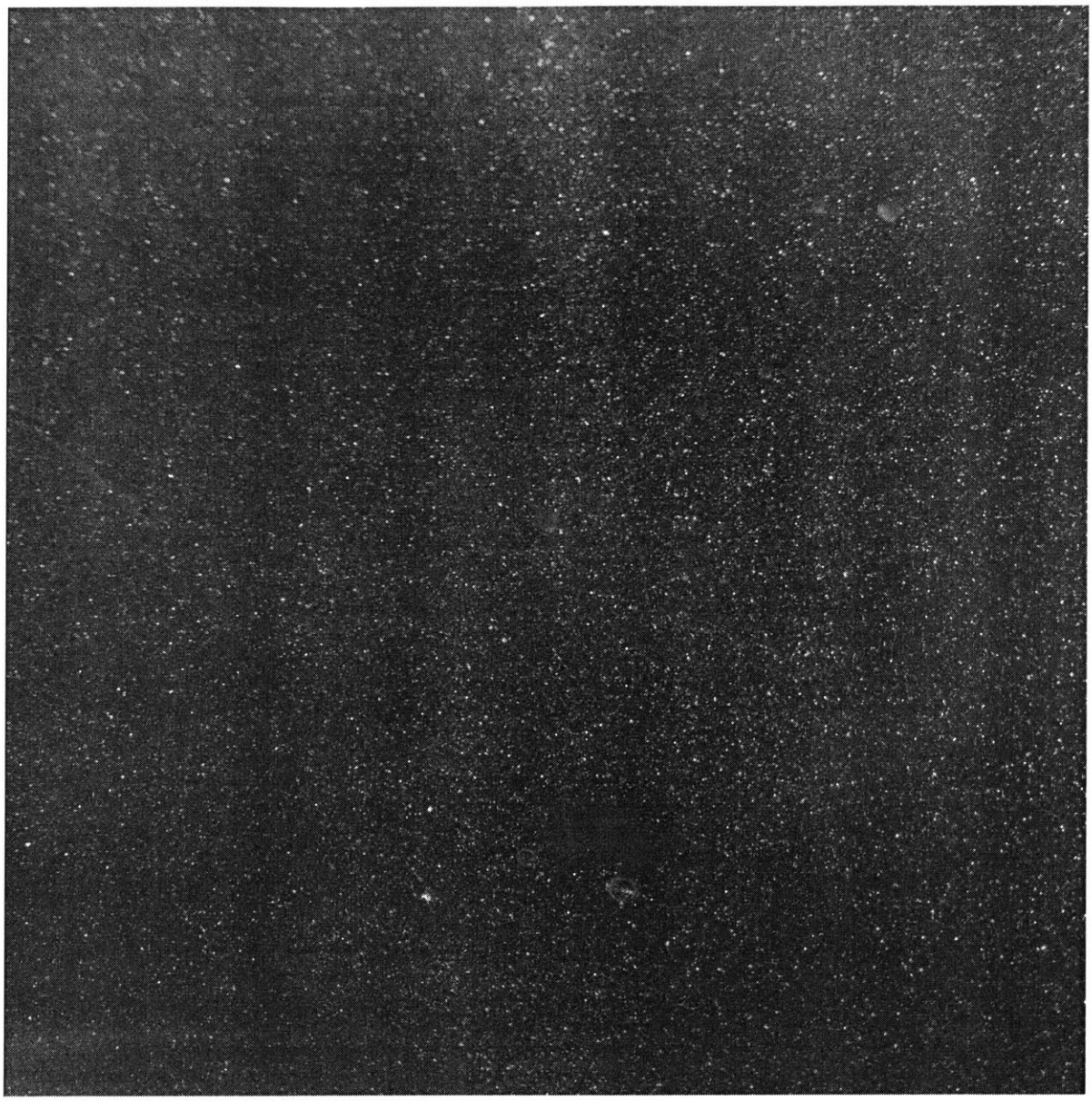

Figure 28 *- PIT Image of Cold Jet entering Hot Tank, 630-nm filtered*

The jet can be seen entering the tank approximately half-way across, at the top of the tank. The images are 1000x1016 pixels, as noted before. The image was analyzed using 32x32 pixel sub-regions and 50% window overlap, using the gradient clipping method. The image intensity ratio contour is shown in Figure 29. Imposed on the contour are the 2-D component of the 3-D velocity vectors calculated with the PIV software.

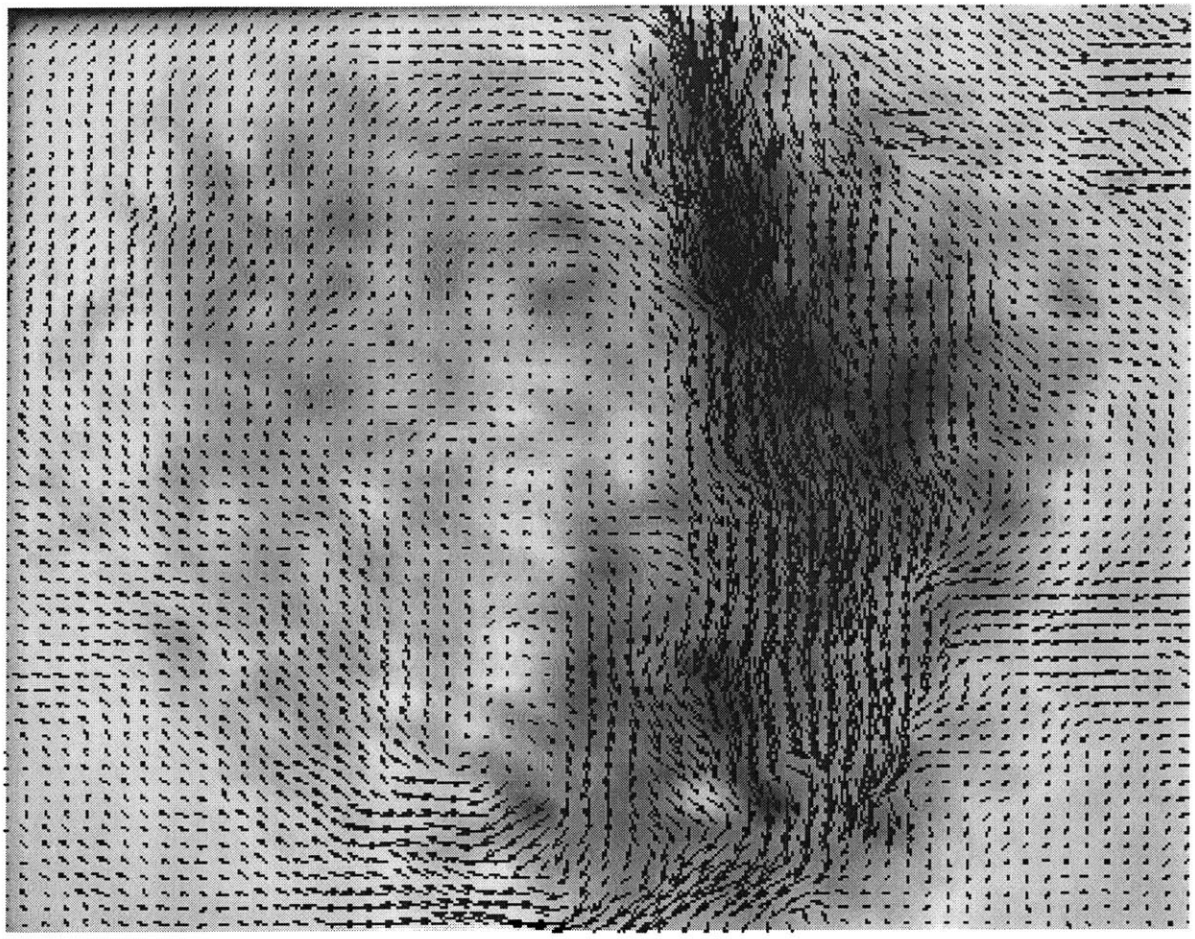

Figure 29 *- Intensity Ratio Contour with 2D Velocity Vectors Superimposed*

A correct intensity ratio-to-temperature calibration was not achieved in the current study due to equipment availability and other limitations. However, the qualitative correlation between velocity and the intensity ratio shown in Figure 29 is strong evidence that the method does indeed work as intended.

Chapter 7 - Conclusions and Recommendations

Advancement of techniques in experimental fluid mechanics is an ongoing science in itself. The development of high quality quantitative techniques for whole-field velocity measurement has dominated an entire aspect of the field for several years. To a lesser extent, quantitative techniques for temperature measurement have also been studied. The current research presented here provides another viable technique for simultaneous measurement of temperature and velocity.

The most efficient and accurate analysis technique developed uses a sub-region intensity average method with gradient level threshold. Window size and overlap is optimized using synthetic images, resulting in a 32x32 pixel window with between 50% and 80% overlap.

Experimental evidence is offered as proof that the technique is viable. While a concrete temperature-intensity correlation was not arrived at, the intensity ratio correlates extremely well with the known velocity vector fields obtained by PIV analysis of the images.

The present thesis has laid the groundwork for several aspects of this technique. Assessment of particle thermal time response, effects of size distribution and aspects of PIT particle manufacturing have been established. PIT image analysis techniques are developed, as well as optimal window size and overlap.

Future work on this technique should include: determination of a precise temperature-intensity ratio correlation, experimental proof of particle thermal time response, and the manufacture of extremely small particles such that the technique can be tested in a different medium such as air.

This technique has much potential in helping the field of experimental fluid mechanics. The understanding of temperature fields is often as important as velocity in many applications, and therefore warrants further development of this experimental technique. The

groundwork presented herein provides a starting point for the future of this technique and the eventual practical use of it in various industrial and academic research environments.

Appendix A - Matlab™ M-file Source Code for Thermal Solution

```
%=========================================================
%
% INTEGRAL3
%
% Calculation of thermal response time of plastic spherical
% particles subjected to pure conduction environment.
%
%
% Uses equation for theta integrated from 0 to R divided by
% volume of sphere to get 'average' value. Stops at a time when
% this value is less than or equal to a % response time indicated
%
% 12/03/98 Alan S. Grissino
%
% 05/21/99 Modified to more accurately computes response time using
%          secant method to zero in on result.
%
% (c)1998 MIT Fluid Mechanics Laboratory
%
clear all
%
% Define diameter
%
%D=50*1e-6;
D=(5:5:75)*1e-6;
%
% Define some physical properties of plastic (Lexan)
%
kp=.19;
cp=.3*4.1868*1e3;
rhop=1.2*998;
a=kp/(rhop*cp);
%kw=0.68;
kw=.0456;
%
% Define time
pct=99;
pc=(1-(pct/100));
ser=1;
disp(sprintf('\n(n = %5d)\n',ser))
disp(sprintf('Particle Size (um)\t%3.0f%% Response Time (ms)',(1-pc)*100))
disp(sprintf('------------------\t------------------------'))
for k=1:length(D),
   R=D(k)/2;
   heff=kw/(R);
   biot=(heff*R)/kp;
   i=1; Av=100; TOL=0.00001 ; t=0.0001;
   typp=0;
   while abs(Av) > TOL,
      C=0;x=0;A=0;X=0;Y=0;
     if typp==1
      for n=1:ser,
         C=((-1)^(n-1))/n*exp(-(n*pi)^2*(a*t/R^2));
         x=n*pi;
         A=1/x;
         X=X+A^2*C*sin(x);
         Y=Y+A*C*cos(x);
      end
      L=X-Y;
      Av=(6/pi)*L-pc;
     else
```

```
      for n=1:ser,
         bi=bessroot2(n,biot);
         C=(1/bi)*((4*(sin(bi)-bi*cos(bi)))/(2*bi-sin(2*bi)))*exp(-bi*a*t/R^2);
         x=bi;
         A=1/x;
         X=X+A^2*C*sin(x);
         Y=Y+A*C*cos(x);
      end
      L=X-Y;
      Av=3*L-pc;
     end
     if i == 1
        t_old=t ; t = t + .01*t ;
        Av_old=Av ; i=i+1 ;
     else
        t_nxt=t-Av*((t-t_old)/(Av-Av_old));
        t_old=t; t=t_nxt ; Av_old=Av ; i=i+1 ;
     end
  end
  nnrt(k)=t;
  disp(sprintf('%14.2f    \t%16.5f',D(k)/1e-6,t/1e-3))
end
junk=0;
if junk==1
plot(D/1e-6,nnrt/1e-3,'b.',D/1e-6,nnrt/1e-3,'k')
title('Particle Thermal Response Time','fontsize',13,'fontweight','bold')
xlabel('Particle Diameter, um')
ystr=sprintf('%3.0f%% Response Time, ms',pct);
ylabel(ystr)
axis([0 100 0 5])
corner(D(9)/1e-6,nnrt(9)/1e-3);
end
```

Appendix B - Matlab™ M-file Source Code for Image Analysis

```
clear all

C=imread('themomit00042ra.tif','tif');
%C=imread('piv_a.tif','tif');
ImR=double(C);clear C;
C=imread('themomit_lrwarp_00042la.tif','tif');
%C=imread('piv_t.tif','tif');
ImL=double(C);clear C;
load cmap.dat;
% Process based on threshold value
B=size(ImR);m=B(1);n=B(2);
p=input('Enter Interrogation Window Size > ');
olpct=input('Enter Window Overlap (%) > ');
ol=1-(olpct/100);
nxwin=floor((floor(m/p)-1)/(ol));
nywin=floor((floor(n/p)-1)/(ol));
po=p-1;
t0 = clock;
disp(sprintf('Processing %7.0f (%4d x %4d) subregions:',nxwin*nywin,nxwin,nywin))
disp(sprintf('using %3d x %3d windows with %3.0f%% overlap\n',p,p,(1-ol)*100))
twin=nxwin*nywin;cpt=0;
for i=1:nxwin
    for j=1:nywin
       cpt=cpt+1;pctcpt=(cpt/twin)*100;
       if mod(pctcpt,5) == 0
          disp(sprintf('Completed %6.0f sub-regions out of %6.0f (%3.0f
%%)',cpt,twin,pctcpt))
       end

     xstart=floor((i*p)-po-p*(i-1)*(1-ol));xend=floor((i*p)-p*(i-1)*(1-ol));
     ystart=floor((j*p)-po-p*(j-1)*(1-ol));yend=floor((j*p)-p*(j-1)*(1-ol));
     GFLAG=0;
     if GFLAG == 0
       IavgL(i,j)=mean(mean(ImL(xstart:xend,ystart:yend)));
       IavgR(i,j)=mean(mean(ImR(xstart:xend,ystart:yend)));
       %IsumL(i,j)=sum(sum(ImL(xstart:xend,ystart:yend)));
       %IsumR(i,j)=sum(sum(ImR(xstart:xend,ystart:yend)));
     elseif GFLAG == 1
      [dxl,dyl]=gradient(ImL(xstart:xend,ystart:yend));
      [dxr,dyr]=gradient(ImR(xstart:xend,ystart:yend));
      dl=sqrt(dxl.^2+dyl.^2);mnl=mean(mean(dl));sigl=mean(std(dl));
      dr=sqrt(dxr.^2+dyr.^2);mnr=mean(mean(dr));sigr=mean(std(dr));
      k=0;l=0;IsumL(i,j)=0;IsumR(i,j)=0;
      for a=1:(xend-xstart)
          for b=1:(yend-ystart)
            if dl(a,b) < (mnl+2*sigl)
               %
            elseif ImL(a+xstart,b+ystart)== 255
               %
            else
               IsumL(i,j)=IsumL(i,j)+ImL(a+xstart,b+ystart);
               k=k+1;
            end
            if dr(a,b) < (mnr+2*sigr)
               %
            elseif ImR(a+xstart,b+ystart)== 255
               %
            else
               IsumR(i,j)=IsumR(i,j)+ImR(a+xstart,b+ystart);
               l=l+1;
            end
          end
      end
```

```
        IavgL(i,j)=IsumL(i,j)/k;
        IavgR(i,j)=IsumR(i,j)/l;
    elseif GFLAG == 3
    % Insert corr function stuff....
    num=0;denom=0;
    for a=1:(xend-xstart)
         for b=1:(yend-ystart)
         q=(ImL(a+xstart,b+ystart)+ImR(a+xstart,b+ystart))-
abs(ImL(a+xstart,b+ystart)-ImR(a+xstart,b+ystart));
         r=(ImL(a+xstart,b+ystart)+ImR(a+xstart,b+ystart));
         num=num+q;denom=denom+r;
         end
     end
     Irat(i,j)=num/denom;
    elseif GFLAG == 4
        avgL=mean(mean(ImL(xstart:xend,ystart:yend)));
        avgR=mean(mean(ImR(xstart:xend,ystart:yend)));
        sigl=mean(std(ImL(xstart:xend,ystart:yend)));
        sigr=mean(std(ImR(xstart:xend,ystart:yend)));
       k=0;l=0;IsumL(i,j)=0;IsumR(i,j)=0;
      for a=xstart:xend
          for b=ystart:yend
            if ImL(a,b) < (avgL+0*sigl)
            %if ImL(a,b) == 0
            % DO NOTHING
            else
               IsumL(i,j)=IsumL(i,j)+ImL(a,b);
               k=k+1;
            end
            if ImR(a,b) < (avgR+0*sigr)
            %if ImR(a,b) == 0
            % DO NOTHING
            else
               IsumR(i,j)=IsumR(i,j)+ImR(a,b);
               l=l+1;
            end
          end
       end
       IavgL(i,j)=IsumL(i,j)/k;
       IavgR(i,j)=IsumR(i,j)/l;
    else
       %IavgL(i,j)=median(nonzeros(sparse(ImL(xstart:xend,ystart:yend))));
       %IavgR(i,j)=median(nonzeros(sparse(ImR(xstart:xend,ystart:yend))));
       IavgL(i,j)=mean(nonzeros(sparse(ImL(xstart:xend,ystart:yend))));
       IavgR(i,j)=mean(nonzeros(sparse(ImR(xstart:xend,ystart:yend))));
    end
    end
end

disp('Completed Processing...')

etime(clock,t0)
Irat=IavgL./IavgR;
Irat2=(Irat./max(max(Irat))).*256;
x2=0.2;x1=1.0;y1=60;y2=140;
TIrat=y1+((y2-y1)/(x2-x1)).*(Irat-x1);

liza=0;
if liza == 0,
  contourf(TIrat(5:nxwin,5:nywin),5);colorbar;set(gca,'Ydir','reverse');axis off
  figure
  pcolor(Irat);shading interp;flipy
  %contourf(Irat,8);flipy;
  %caxis([.8 1.2]);colorbar
  %pcolor(TIrat);shading interp;flipy;caxis([75 150])
  %load xl.dat;load yl.dat;load vxl.dat;load vyl.dat;
  %hold on
```

```
  %quiver(xl,yl,vxl,vyl,5);
else
  ctrp=300/512;pn=nxwin*ctrp;
  %hold on;plot(pn,pn,'ko');
  [y,i]=min(Irat);[z,j]=min(y);col=j;row=i(col);
  %plot(row,col,'bo');
  %r=sqrt((abs(row-pn))^2+(abs(col-pn))^2);r=r/nxwin;
  %disp(sprintf('Window Size: %d  OL: %f  Delta: %f\n',p,(1-ol)*100,r))
  %=================================================================
  % CREATE GUASSIAN PROFILE TO COMPARE TO RESULTS
  locy=300*nywin/512;locx=300*nxwin/512;
  siz=100*nxwin/512;
  drat=0.8;
  %rmat(1:nxwin,1:nywin)=1;
  tx1=floor(locx-siz);tx2=floor(locx+siz);
  ty1=floor(locy-siz);ty2=floor(locy+siz);
  n=0;
  %for m=1:0.01:nxwin
  %n=n+1;
  %   x(n)=m;
  %   gx(n)=1-drat*exp(-(locx-m)^2/siz^2);
  %end
%
%lets do it for the same y loc, at n=locy.
n=0;m=0;p=0;q=0;clear rmat;x=0;y=0;
% This works 8/3/99
%for m=tx1:(tx2-tx1)/50:tx2
%   p=p+1; x(p)=m; q=0;
%   for n=ty1:(ty2-ty1)/50:ty2
%      q=q+1; y(q)=n;
%      rmat(p,q)=1-drat*exp(-((locx-m)^2+(locy-n)^2)/siz^2);
%   end
%end
  %hold off
  %plot(Irat(:,col),'bo');
  col=floor(locy);
  for m=1:length(Irat(:,col))
     n=m;
     x(n)=m;
     if m <= tx1
        gx(m)=Irat(m,col);
     elseif m >=tx2
        gx(m)=Irat(m,col);
     else
        gx(m)=1-drat*exp(-(locx-m)^2/siz^2);
     end
     delt(m)=gx(m)-Irat(m,col);
  end
  %plot(Irat(:,locy),'bo');
  %hold on;plot(x,rmat(:,m/2),'r-');
  plot(x,delt,'k^');
  %plot(x(tx1+1:tx2-1),gx(tx1+1:tx2-1),'k-');hold on;plot(Irat(:,col),'ko');
  %figure;contour(x,y,rmat);flipy
  %hline(1-drat,1)
  %vline(pn);hline(0,0);axis([0 nxwin -0.5 0.5]);
end
```

Appendix C – Derivation of Volume Averaged Temperature Response

This appendix outlines the mathematical procedure behind the derivation of the volume averaged temperature response. Although the four (4) solutions are different depending on the assumed boundary conditions, the math used to solve the volume average is the same or very similar. Shown below is an example of the derivation for the *Sphere in Contact with a Well Stirred Fluid* method, per Section 4.2.2.3.

First, the base equation is restated for clarity.

$$T(r,t)=\frac{T_o}{\varepsilon+1}-\frac{2\varepsilon R T_o}{3r}\cdot\sum_{n=1}^{\infty}\left\{e^{-\alpha\beta_n^2 t}\cdot\frac{\varepsilon^2(R\beta_n)^4+3\cdot(2\varepsilon+3)\cdot(R\beta_n)^2+9}{\varepsilon^2(R\beta_n)^4+9\cdot(\varepsilon+1)\cdot(R\beta_n)^2}\cdot\sin(R\beta_n)\cdot\sin(r\beta_n)\right\} \tag{33}$$

Expressed in terms of the normalized temperature, Θ,

$$\Theta(r,t)=1+\frac{2(\varepsilon+1)R}{r}\cdot\sum_{n=1}^{\infty}\left\{e^{-\alpha\beta_n^2 t}\cdot\frac{\varepsilon^2(R\beta_n)^4+3\cdot(2\varepsilon+3)\cdot(R\beta_n)^2+9}{\varepsilon^2(R\beta_n)^4+9\cdot(\varepsilon+1)\cdot(R\beta_n)^2}\cdot\sin(R\beta_n)\cdot\sin(r\beta_n)\right\} \tag{59}$$

Now the volume averaging equation is introduced, as in the text body.

$$\Theta(t)_{AVG}=\frac{4\pi\int_0^R\Theta(r,t)r^2dr}{\frac{4}{3}\pi R^3} \tag{10}$$

or

$$\Theta(t)_{AVG}=\frac{3}{R^3}\cdot\int_0^R\Theta(r,t)r^2dr \tag{60}$$

Inserting Equation (59) into Equation (60),

$$\Theta(t)_{AVG} = \frac{3}{R^3} \cdot \int_0^R \left[1 + \frac{R}{r}(2(\varepsilon+1)) \sum_{n=1}^{\infty} A_n B_n \sin(r\beta_n) \right] r^2 dr \tag{61}$$

where A_n and B_n are defined below, since neither depends upon r.

$$A_n = \frac{\varepsilon^2 (R\beta_n)^4 + 3 \cdot (2\varepsilon+3) \cdot (R\beta_n)^2 + 9}{\varepsilon^2 (R\beta_n)^4 + 9 \cdot (\varepsilon+1) \cdot (R\beta_n)^2} \cdot \sin(R\beta_n), \tag{62}$$

and

$$B_n = e^{-\alpha\beta_n t}. \tag{63}$$

First, the integral part of Equation (61) is solved. Let this integral term be called P. Distributing the r^2 term inside the brackets, P becomes,

$$P = \int_0^R \left[r^2 + 2Rr(\varepsilon+1) \sum_{n=1}^{\infty} A_n B_n \sin(r\beta_n) \right] dr \tag{64}$$

Splitting this integral term,

$$P = \int_0^R r^2 dr + \int_0^R 2Rr(\varepsilon+1) \sum_{n=1}^{\infty} A_n B_n \sin(r\beta_n)\, dr \tag{65}$$

The first integral in P is solved simply, as

$$\int_0^R r^2 dr = \frac{r^3}{3}\Big|_0^R = \frac{R^3}{3}. \tag{66}$$

For the second term in P, we begin by pulling anything constant with respect to r out of the integrand, as

$$2R(\varepsilon+1) \cdot \int_0^R r \sum_{n=1}^{\infty} A_n B_n \sin(r\beta_n)\, dr \tag{67}$$

The integral expressed in Equation (67) can be solved using integration by parts. Integration by parts is defined as

$$\int u\,dv = uv - \int v\,du \tag{68}$$

Using this definition, we define the parts of Equation (67) by

$$2R(\varepsilon+1)\cdot\int_0^R \underbrace{r}_{u}\underbrace{\sum_{n=1}^{\infty} A_n B_n \sin(r\beta_n)\,dr}_{dv} \tag{69}$$

So, since

$$u \equiv r \qquad \Rightarrow \qquad du = dr \tag{70}$$

and

$$dv = \sum_{n=1}^{\infty} A_n B_n \sin(r\beta_n)\,dr \qquad \Rightarrow \qquad v = \int dv = \int \sum_{n=1}^{\infty} A_n B_n \sin(r\beta_n)\,dr \tag{71}$$

Solving this integral,

$$v = -\sum_{n=1}^{\infty} \frac{A_n B_n}{\beta_n} \cos(r\beta_n) \tag{72}$$

Furthermore, the integral of *vdu* as required by Equation (68) is

$$\int v\,du = \int -\left[\sum_{n=1}^{\infty} \frac{A_n B_n}{\beta_n} \cos(r\beta_n)\right] dr = -\sum_{n=1}^{\infty} \frac{A_n B_n}{\beta_n^2} \sin(r\beta_n) \tag{73}$$

Inserting Equation (70), (72) and (73) back into Equation (68),

$$\int u\,dv = uv - \int v\,du = r\cdot\left[-\sum_{n=1}^{\infty} \frac{A_n B_n}{\beta_n} \cos(r\beta_n)\right] - \left[-\sum_{n=1}^{\infty} \frac{A_n B_n}{\beta_n^2} \sin(r\beta_n)\right] \tag{74}$$

Evaluating the integrals from 0 to R and rearranging, we get,

$$\left[\sum_{n=1}^{\infty} \frac{A_n B_n}{\beta_n^2} \sin(R\beta_n)\right] - R\sum_{n=1}^{\infty} \frac{A_n B_n}{\beta_n} \cos(R\beta_n) \tag{75}$$

Therefore, substituting Equation (75) back into (69) and again into Equation (65), we get the integral P solved as,

$$P = \frac{R^3}{3} + 2R(\varepsilon+1)\left\{\sum_{n=1}^{\infty}\frac{A_n B_n}{\beta_n^2}\sin(R\beta_n) - R\sum_{n=1}^{\infty}\frac{A_n B_n}{\beta_n}\cos(R\beta_n)\right\} \tag{76}$$

Substituting the integral term P back into Equation (61), along with some trigonometric manipulation, we get

$$\Theta(t)_{AVG} = 1 + \frac{6(\varepsilon+1)}{R^2}\left\{\sum_{n=1}^{\infty}\frac{a_n B_n}{\beta_n^2}\sin^2(R\beta_n) - R\sum_{n=1}^{\infty}\frac{a_n B_n}{\beta_n}\sin(2R\beta_n)\right\} \tag{77}$$

where,

$$a_n = \frac{\varepsilon^2(R\beta_n)^4 + 3\cdot(2\varepsilon+3)\cdot(R\beta_n)^2 + 9}{\varepsilon^2(R\beta_n)^4 + 9\cdot(\varepsilon+1)\cdot(R\beta_n)^2} \tag{78}$$

With slight manipulation, Equation (77) and (78) are equivalent to the Equation (39) in the text.

Each of the four modeling methods contains this similar form for the volume average equation. Although the specific equations are different, each is volume averaged using integration by parts and other trigonometry and calculus manipulations.

References

1. Ogden, T.R.; Hendricks, E.W., (1984) "Liquid Crystal Thermography in Water Tunnels", *Experiments in Fluids* Vol. 2, pp. 65

2. Rhee, H.S.; Koseff,J.R.; Street, R.L. (1984), "Flow Visualization of a Recirculating flow by Rheoscopic Liquid and Liquid Crystal Techniques", *Experiments in Fluids*, Vol. 2, pp. 57

3. Dabiri, D; Gharib, M., (1991), "Digital Particle Image Thermometry and its Application to a Heated Vortex-Ring", *5th Int. Symp. on Appl. of Laser Tech. to Fluid Mechanics*, Lisbon. pp 82-101

4. Nakajima T; Utsunomiya M; Ikeda Y (1991), "Simultaneous Measurement of Velocity and Temperature of Water Using LDV and Fluorescence Technique", *5th Int. Symp. on Appl. of Laser Tech. to Fluid Mechanics*, Lisbon. pp 36-53

5. Coppeta, J; Rogers C. (1998), "Dual Emission Laser Induced Fluorescence for Direct Planar Scalar Behavior Measurements"

6. Sakakibara, J; Adrian, R.J. (1999), "Whole Field Measurement of Temperature in Water using Two-color Laser Induced Fluorescence", *Experiments in Fluids* Vol. 7, pp. 15

7. Bassnett, S; Reinisch, L; Beebe, D. (1990), "Intracellular pH Measurement Using Single Excitation-Dual Emission Fluorescence Ratios", *Am. J. of Physiology*, 258, C171

8. Morris, S.J. (1990), "Real-Time Mulit-Wavelength Fluorescence Imaging of Living Cells", *BioTechniques* Vol. 8, pp 296

9. Parker,W.J., et al., (1993), "Fiber-Optic Sensors for pH and Carbon Dioxide Using a Self-Referencing Dye", *Analytical Chemistry*, Vol. 65, pp. 2329

10. Frigerio, F. (1997), "Velocity Field Measurements of a Jet Confined to a Swirling Flow Using Digital Particle Image Velocimetry Cinematography", Masters Thesis, Massachusetts Institute of Technology.

11. Carslaw, H.S., and Jeager, J.C., Conduction of Heat in Solids, © 1959 Oxford Press, pp. 240, 351

12. Schneider, P.J., Conduction Heat Transfer, c 1955 Addison-Wesley Publishing Co., pp. 229-257

13. Whitaker, S., (1972), "Forced Convection Heat Transfer Correlations for Flow in Pipes, Past Flat Plates, Single Cylinders, Single Spheres, and Flow in Packed Beds and Tube Bundles," *AIChE*

Journal, Vol. 18, pp 361-371.

14. Heisler, M.P. (1947), "Temperature Charts for Induction and Constant Temperature Heating", *ASME Transactions*, Vol 69, pp. 227-236

15. Hart, D.P. (1996), "Sparse Array Image Correlation." 8th International Symposium on Applications of Laser Techniques to Fluid Mechanics", Lisbon Portugal.

16. White, F.M.; Heat and Mass Transfer, © 1991Addison-Wesely Publishing